Opposition flow control for reducing skin-friction drag of a turbulent boundary layer

Dacome, Giulio; Mörsch, Robin; Kotsonis, Marios; Baars, Woutijn J.

DOI
10.1103/PhysRevFluids.9.064602

Publication date
2024

Document Version
Final published version

Published in
Physical Review Fluids

Citation (APA)
Dacome, G., Mörsch, R., Kotsonis, M., & Baars, W. J. (2024). Opposition flow control for reducing skin-friction drag of a turbulent boundary layer. *Physical Review Fluids*, *9*(6), Article 064602. https://doi.org/10.1103/PhysRevFluids.9.064602

PHYSICAL REVIEW FLUIDS **9**, 064602 (2024)

Opposition flow control for reducing skin-friction drag of a turbulent boundary layer

Giulio Dacome,[1,*] Robin Mörsch,[2] Marios Kotsonis,[1,†] and Woutijn J. Baars[1,‡]
[1]*Faculty of Aerospace Engineering, Delft University of Technology, 2629 HS Delft, The Netherlands*
[2]*Institute of Applied Mathematics and Scientific Computing, University of the Bundeswehr Munich, 85577 Neubiberg, Germany*

(Received 6 September 2023; accepted 12 April 2024; published 6 June 2024)

This work explores the dynamic response of a turbulent boundary layer to large-scale reactive opposition control, at a friction Reynolds number of $\mathrm{Re}_\tau \approx 2\,240$. A surface-mounted hot-film is employed as the input sensor, capturing large-scale fluctuations in the wall-shear stress, and actuation is performed with a single on/off wall-normal blowing jet positioned 2.4δ downstream of the input sensor, operating with an exit velocity of $v_\mathrm{j} = 0.4U_\infty$. Our study builds upon the work of Abbassi *et al.* [Int. J. Heat Fluid Flow **67**, 30 (2017)] and includes a control-calibration experiment and a performance assessment using PIV- and PTV-based flow field analyses. With the control-off calibration-experiment conducted *a priori*, a transfer kernel is identified so that the velocity fluctuations that are to-be-controlled can be estimated. The controller targets large-scale high-speed zones in an "opposing" mode and low-speed zones in a "reinforcing" mode. A desynchronized mode was tested for reference and consisted of a statistically similar control mode, but without synchronization to the incoming velocity fluctuations. An energy-attenuation of about 40 % is observed for the opposing control mode in the frequency band corresponding to the passage of large-scale motions. This proves the effectiveness of the control in targeting large-scale motions: an energy-intensification of roughly 45% occurs for the reinforcing control mode instead, while no change in energy, within the wall-normal range targeted, appears with the desynchronized control mode. Moreover, direct measures of the skin-friction drag are inferred from PTV data. Results indicate that the opposing control logic yields the lowest wall-shear stress (3% lower than the desynchronized control, and 10% lower than the uncontrolled flow). Finally, a FIK-decomposition of the skin-friction coefficient revealed that the off-the-wall turbulence follows a consistent trend with the PTV-based wall-shear stress measurements, although biased by an increased shear in the wake of the boundary layer given the formation of a plume due to the jet-in-crossflow actuation.

DOI: 10.1103/PhysRevFluids.9.064602

---

[*] g.dacome@tudelft.nl
[†] m.kotsonis@tudelft.nl
[‡] w.j.baars@tudelft.nl

I. INTRODUCTION

Strategies to control friction of wall-bounded turbulence rely on the fundamental understanding of boundary layer flows and their friction-generating mechanisms. Research has revealed how different coherent structures exist, and how the structures' characteristics vary as a function of wall-normal distance, particularly when considering their sizing and spatiotemporal dynamics [1–5]. In the inner region, structures scale with the viscous length scale ν/U_τ, and timescale ν/U_τ^2, with ν being the kinematic viscosity and $U_\tau \equiv \sqrt{\tau_w/\rho}$ being the friction velocity (τ_w is the wall-shear stress and ρ is the fluid density). In the outer region, instead, structures scale with the boundary layer thickness δ as the characteristic lengthscale and δ/U_∞ as timescale, with U_∞ now being the free-stream velocity. The ratio of outer to inner length scales is provided by the friction Reynolds number, which is defined as $\mathrm{Re}_\tau \equiv \delta U_\tau/\nu$.

When focusing on control, a large number of studies aim at manipulating the near-wall cycle (NWC) dynamics [6–10] and this generally leads to a disruption of the turbulence production cycle in the inner region [11–13]. For engineering systems of practical relevance, friction Reynolds numbers are in the order of $\mathcal{O}(10^3)$ to $\mathcal{O}(10^6)$. Corresponding physical time and length scales would result in an unfeasible number of streamwise control stations for achieving streamwise-persistent control when targeting the NWC scales. For this reason, our work focuses on control of large-scale structures with the aid of a discrete sensor-actuator layout. Schoppa and Hussain [14] were the first to introduce such large-scale control. They showed that large-scale spanwise velocity forcing could lead to a 50% reduction in friction drag. However, the relatively low Reynolds number of $\mathrm{Re}_\tau \approx 180$ implied that: (1) control was effectively targeting a weak instability as turbulence was only marginally sustained [15,16], and (2) large-scale control at those low values of Re_τ was matching the NWC dynamics. That is, in the context of practical applications, a large-scale control strategy requires a high-enough Reynolds number for sufficient scale separation to appear. This is conveniently achieved through experimental studies. With increasing Re_τ, large-scale motions (LSMs) contribute more and more to the total turbulence kinetic energy (TKE), while the contribution of small scales remains constant [17]. LSMs refer to regions of lower velocity induced between the legs of hairpin packets, and regions of higher velocity outside of said packets. Due to the streamwise momentum difference between high- and low-speed zones, large-scale rollers are formed with a downwash and upwash in the zones with a momentum surplus and deficit, respectively [18].

Recently, predetermined control with large-scale forcing was proven effective at high Re_τ [17,19] and the inherent lower-frequency nature of outer scales also renders LSMs a more approachable target than inner scales. Even when exclusively actuating upon larger scales, the intensity of the NWC can still be affected through a modulation phenomenon: large-scale outer layer structures condition the dynamics in the near-wall region of high-Reynolds-number flows [20,21]. Subsequently, the mean velocity gradient at the wall is altered and so is the mean wall-shear stress, $\tau_w = \mu \partial \overline{u}/\partial y|_{y=0}$ (here μ is the dynamic viscosity of the flow and $\overline{u}$ is the mean streamwise velocity).

Opposition control is a type of *stabilizing control* [22] that was initially applied to turbulent flows in the context of computational investigations. This technique proved rather effective in suppressing turbulent fluctuations and even reducing skin-friction drag [23,24]. However, full observability of the fluid system and straightforward access to boundary conditions, which are inherent in numerical simulations, result in ample control authority. In an experimental setting, observability is limited and actuation has to be performed at discrete spatial locations. This type of control was pioneered experimentally in the works of Robbek and Choi [25,26]. Abbassi *et al.* [27] demonstrated a selective opposition control system to target LSMs carrying higher streamwise momentum than average, in an attempt to reduce the skin-friction drag induced by large-scale events in a TBL at $\mathrm{Re}_\tau \approx 14\,000$. A spanwise array of jet actuators, together with hot-film input sensors located upstream, counteracted the naturally occurring drag-producing LSMs. This yielded a reduction of the intensity of the velocity fluctuations in the logarithmic region, as well as a ≈3% reduction in the mean wall-shear stress.

Our current work builds upon the approach taken by Abbassi *et al.* [27]: the momentum surplus that characterizes high-speed zones is to be counteracted by lower-streamwise-momentum fluid, generated by a wall-normal blowing jet actuator. To minimize the parasitic drag associated with the control system, wall-embedded flush-mounted hardware is required. This constraint leads to an estimation problem of the flow state at a point away from the input sensor when aiming at the manipulation of large-scale structures at their wall-normal location of maximum intensity (e.g., in the geometric center of the logarithmic region). Fortunately, LSMs present a large degree of wall-coherence [28], e.g., a measurable imprint on the wall in the form of a low-frequency component. Still, the question remains as to how accurate estimations of the flow state at a location above the actuator can be performed. Abbassi *et al.* [27] took Gaussian kernels as transfer functions and convolved those with the input signals. In the present work, we employ a data-driven approach to obtain the input-output relation, namely to relate changes in wall-shear fluctuations to velocity fluctuations in the logarithmic region. Using spectral linear stochastic estimation (LSE) [29,30], we are able to generate such a physics-informed kernel. The principal goal of this article, in further contrast to the work of Abbassi *et al.* [27], is to relate changes in the mean skin-friction drag to changes in the turbulence statistical integral measures of the TBL flow as a result of control in an attempt to unravel the physical mechanisms underlying changes in skin friction. For zero-pressure-gradient (ZPG) uncontrolled TBL flows this has been detailed by Renard and Deck [31] and Deck *et al.* [32]; they relate integral measures of the TKE production (and a FIK decomposition [33] of the turbulent flow field) to the mean wall-shear stress. While it is known from aformentioned studies that the chosen actuator (a wall-normal blowing jet) can potentially reduce skin-friction drag, the goal of this work is to analyze the variation of wall-shear stress as a function of the chosen control mode (i.e., of reactive, real-time actuation targeting drag-producing large-scale structures). With a unique experimental dataset we will examine the relation of such integral measures of the flow to the mean wall-shear stress downstream of our control-action.

The article is outlined as follows. The experimental arrangement is presented in Sec. II, after which the control system is described in Sec. III. Details of the response of the TBL flow to several control modes are analysed in Sec. IV, and Sec. V follows with an assessment of the skin-friction drag, as well as its relation to integral properties of the TBL flow.

II. EXPERIMENTAL METHODOLOGY

A. Turbulent boundary layer setup

Experiments were carried out in an open-return wind tunnel facility (W-Tunnel) at the Delft University of Technology. This facility has a contraction ratio of 4:1, with a square cross-sectional area of $0.6 \times 0.6\,\mathrm{m}^2$ at the inlet of the test section. Driven by a centrifugal fan, the flow at the test section's inlet can reach a velocity of up to $\approx 16.5\,\mathrm{m/s}$.

For generating a TBL at a Reynolds number of practical significance, a test section with a relatively long flat plate was used of 3.75 m in length and 0.60 m in width. A schematic representation of the setup is shown in Fig. 1(a). The boundary layer is tripped on all four walls of the test section's inlet, with a 0.12-m-long strip of P40-grain sandpaper. A global right-handed Cartesian coordinate system (x', y', z') is defined with its origin at the wall, in the spanwise center of the test section and coinciding with the downstream edge of the trip. A second coordinate system (x, y, z) is used for presenting results in later sections, and has its origin at the jet actuator's center. Control hardware, comprising a surface-mounted hot-film and a wall-normal blowing jet actuator, were integrated in the floor panel. The hot-film was placed at $x' = 2.73\,\mathrm{m}$ ($x = -0.17\,\mathrm{m}$), while the actuator was situated downstream of that at $x' = 2.90\,\mathrm{m}$ ($x = 0$). Specifications of the sensor and actuator, and reasons for their placement, are provided in Sec. III.

A Pitot-static probe is integrated on a side wall of the test section to provide a velocity reading at $x' = 2.90\,\mathrm{m}$ and $y' = 0.40\,\mathrm{m}$. The tunnel's ceiling was made adjustable in height over the full length of the test section to modify the streamwise pressure gradient, $\partial p/\partial x$. The ceiling consists of a

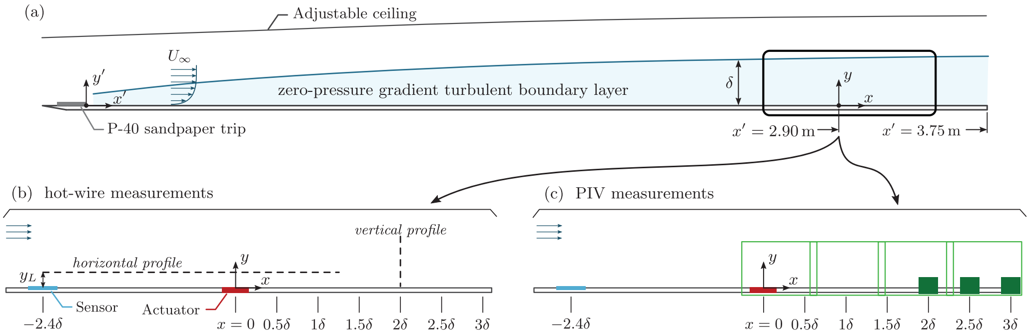

FIG. 1. (a) Schematic of the turbulent boundary layer test section at the Delft University of Technology. (b) Schematic indicating the locations of hot-wire measurements, with a streamwise profile taken at $y_L^+ = 3.9\sqrt{\mathrm{Re}_\tau}$ and a wall-normal profile taken at $x = 2\delta$. (c) Positions of the fields of view for PTV (filled dark green) and PIV (open light green) measurements.

4-mm-thick polycarbonate plate with a smooth curvature. Through an iterative process, the ceiling was configured for a ZPG that was characterized using two streamwise rows of static pressure taps in the floor (at $z' = \pm 0.20\,\mathrm{m}$). For the nominal free-stream velocity of the current study ($U_\infty \approx 15\,\mathrm{m/s}$), the acceleration parameter $K \equiv (\nu/U_e^2)(dU_e/dx)$ [34] remained in an acceptable range for a ZPG condition, since $K < 1.6 \times 10^{-7}$ for the entire length of the test section. In the definition of K, the velocity at the edge of the boundary layer, U_e, equals U_∞; its value was inferred from the measured static pressure at the wall by assuming $\partial p/\partial y \approx 0$. Finally, the free-stream turbulence intensity was found to be $\sqrt{\overline{u^2}}/U_\infty \approx 0.35\,\%$ at the primary measurement region around $x = 0$ (this was inferred using hot-wire anemometry, described later).

B. Measurement instrumentation

Time series of the streamwise velocity component were acquired using Hot-Wire Anemometry (HWA). A TSI IFA-300 Constant Temperature Anemometer (CTA) was used, with a standard Dantec 55P15 boundary layer probe. Data were sampled at a rate of $f_{\mathrm{HW}}^+ = 3.16$ ($f_{\mathrm{HW}} = 51.2\,\mathrm{kHz}$) with a 24-bit A/D conversion for an uninterrupted duration of $T_a = 150\,\mathrm{s}$ at each measurement point. This acquisition duration equates to $T_a U_\infty/\delta \approx 32\,000$ boundary layer turnover times; this was checked to be sufficient for converged spectral statistics at the lowest frequencies of interest. The hot-wire was calibrated in-situ by fitting King's Law to 17 points of increasing velocity. Measurement time series were corrected for temperature drift following the procedure outlined by Hultmark and Smits [35]. By mounting the probe to a dual-axis traversing system, with a step accuracy of 10 μm (smaller than 0.3 viscous units), a wall-normal profile consisting of 40 logarithmically spaced points was acquired at $x = 2\delta$. A streamwise profile was also measured within the geometric center of the logarithmic region, at a location of $y_L^+ = 3.9\sqrt{\mathrm{Re}_\tau} \approx 190$ ($y_L = 6.3\,\mathrm{mm}$), see Fig. 1(b). The uncertainty in the hot-wire measurements was computed following the procedure of Smith *et al.* [36], and resulted in uncertainties in the estimation of the average velocity and standard deviation (at $y^+ \approx 15$) of 0.26 % and 1.02 %, respectively.

Planar particle tracking velocimetry (PTV) data were acquired with a field of view (FOV) of approximately $0.33\delta \times 0.28\delta$. A relatively small FOV was chosen to maximise the resolution in the viscous sub-layer, such that the wall-shear stress could be inferred directly from the velocity gradient at the wall, $\tau_w = \mu \partial \bar{u}/\partial y|_{y=0}$ (see Sec. V A). Particle image velocimetry (PIV) was also employed in a planar two-dimensional two-component (2D2C) configuration, with a larger FOV spanning approximately $3.6\delta \times 0.8\delta$ (divided over two cameras). This PIV campaign was tailored to studying the flow well into the wake of the boundary layer. For both the PTV and PIV measurements, data were acquired at several streamwise locations, indicated in Fig. 1(c) with the blue filled

TABLE I. Image acquisition parameters for the PTV and PIV campaigns, with dt being the time separation between images in one pair, and l_f and $f_\#$ the focal length and f-stop of the camera lens.

Campaign	FOV size	No. of cameras	dt (µs)	l_f (mm)	$f_\#$	Pixel res. (pix/mm)	Particle size (pix)
PTV	$0.33\delta \times 0.28\delta$	1	15	200	11	114	5
PIV	$3.6\delta \times 0.8\delta$	2	35	105	8	18	3

rectangles (for PTV) and the green open rectangles (for PIV). Table I lists the acquisition parameters for both the PTV and PIV campaigns. LaVision Imager sCMOS cameras with a sensor size of $2650 \times 2160\,\text{pix}^2$ were used in both types of acquisitions. All measurement sets comprised a total of 2000 statistically independent image pairs that were recorded at a frequency of 15 Hz. Illumination was provided by a Quantel Evergreen 200 Nd:YAG laser, operating in double-pulse mode with a maximum energy per pulse of 125 mJ. Finally, seeding was generated by an atomized glycol-water mixture, yielding an average particle size of ≈1 µm.

C. Turbulent boundary layer characteristics

A characterization of the uncontrolled TBL flow at the primary measurement location of $x' = 2.90\,\text{m}$ is here reported, based on first- and second-order statistics computed from hot-wire data. Figure 2(a) presents profiles of both the streamwise mean velocity and TKE. A set of canonical boundary layer parameters was inferred through a composite fit procedure on the mean velocity profile [37], with logarithmic layer constants of $\kappa = 0.38$ and $B = 4.7$. Parameters are reported in Table II. Here, θ is the momentum thickness and Π is the wake parameter. The viscous length scale is denoted with symbol l^*. Since the measured streamwise TKE is subject to a well-known attenuation of small-scale energy, associated with the the finite resolution of the hot-wire sensing

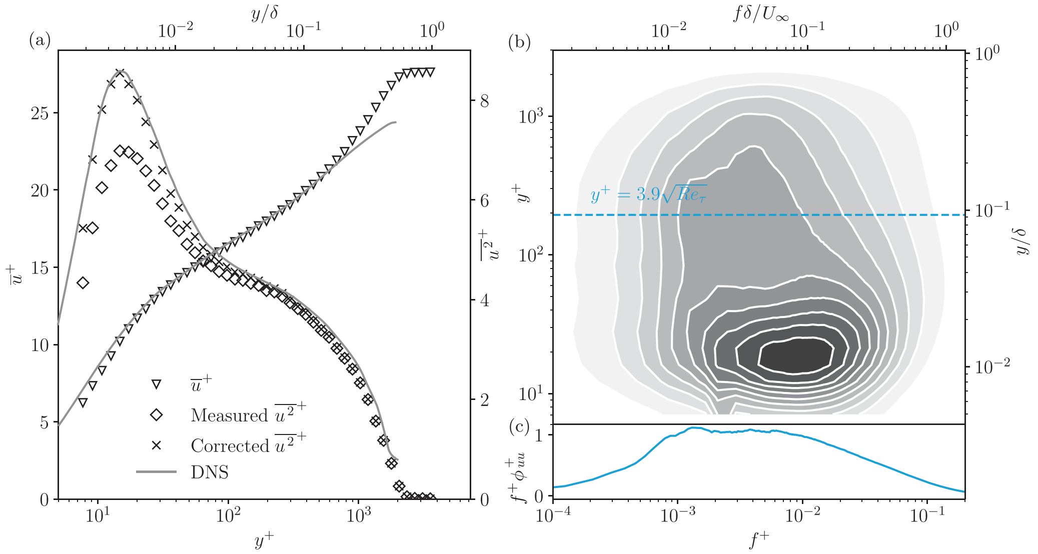

FIG. 2. (a) Wall-normal profiles of the mean streamwise velocity and streamwise TKE, based on hot-wire data and compared to DNS data of channel flow at $\text{Re}_\tau = 2\,000$ [40]. TKE corrected for attenuation due to sensor resolution [39]. (b) Premultiplied energy spectrogram of the streamwise velocity; filled isocontours correspond to magnitudes of 0.2:0.2:2.2. (c) Energy spectrum of the streamwise velocity fluctuations in the geometric center of the logarithmic region, $y_L^+ = 3.9\sqrt{\text{Re}_\tau}$.

TABLE II. Experimental parameters of the baseline TBL flow in the W-Tunnel facility at $x' = 2.90\,\mathrm{m}$ ($x = 0$).

U_∞ (m/s)	δ (mm)	θ (mm)	Re_θ	U_τ (m/s)	Re_τ	Π	$l^* \equiv \nu/U_\tau$ (μm)	ν/U_τ^2 (μs)
15	69.9	6.83	6 830	0.49	2 237	0.61	31.25	65.10

element ($l^+ \approx 41$) [38], the missing energy can be accounted for as seen from the corrected measurement profile following Ref. [39]. For both the mean velocity and corrected streamwise TKE profiles, the measurement data compare well to those of a direct numerical simulation (DNS) of channel flow [40] in the inner region and at a comparable value of Re_τ. This provides reassurance of a representative baseline flow.

For spectral analyses of the velocity $u(y, t)$, the one-sided spectrum is taken as $\phi_{uu}(y; f) = 2\langle U(y; f)U^*(y; f)\rangle$, where $U(y; f) = \mathcal{F}[u(y, t)]$ is the temporal fast Fourier transform (FFT). Here the angular brackets $\langle\cdot\rangle$ denote ensemble-averaging and the superscript $*$ signifies the complex conjugate. Ensembles of $N = 2^{17}$ samples were subject to a Hanning windowing procedure, and resulted in a spectral resolution of $df = 0.39\,\mathrm{Hz}$. In addition, a 50 % overlap was implemented to yield a total of 120 ensembles for averaging. Energy spectra throughout the TBL flow are premultiplied, and are presented as an inner-scaled spectrogram, $f^+\phi^+_{uu}(y; f)$, in Fig. 2(b). The Reynolds number being relatively low does not yet allow for a noticeable outer-spectral peak to appear, but the inner-spectral peak is apparent at $(y^+; f^+) \approx (15; 0.01)$. Moreover, a significant scale separation is present between energetic motions in the outer layer (say at $f^+ \lesssim 10^{-3}$) and the NWC peak at $f^+ \approx 10^{-2}$. The uncontrolled TBL conditions reported in Table II and Fig. 2 represent the baseline (uncontrolled) case, which the controlled flow will be compared to in subsequent sections.

III. CONTROL SYSTEM ARCHITECTURE

From a high-level perspective, the control system consists of a wall-embedded sensor and actuator, and a real-time target machine. Downstream flow measurements are performed to assess the controller's performance. For the controller to be effective, it is critical for the input sensor to provide sufficient information to estimate the state of the to-be-controlled plant (i.e., the TBL flow). Similarly, the actuator is required to have enough control authority to generate a significant effect in the logarithmic region, where the large-scale structures are most energetic.

A. Wall-based sensing and actuation

Our control logic aims at actuating upon structures that convect in the logarithmic region and that leave a footprint at the wall [20,30]. Similar to Abbassi *et al.* [27], a Dantec 55R47 glue-on hot-film was selected as the surface-mounted input sensor. Its sensing element measures 0.1 mm in the streamwise direction ($\delta x^+_{\mathrm{HF}} = 3.2$) and 0.9 mm ($\delta z^+_{\mathrm{HF}} = 28.8$) in the spanwise one. The sensor is deposited on a ≈50 μm thick ($1.6l^*$) KaptonT foil. This thickness makes the hot-film a nonintrusive sensor, since it can be considered hydrodynamically smooth. The sensor was glued in the spanwise center at $x = -2.4\delta$ ($x = -0.17\,\mathrm{m}$), to a polycarbonate insert within the floor (see Fig. 1). Its lead-wires were routed downstream and out of the tunnel through 0.4 mm diameter holes.

The hot-film was operated using a second CTA channel in the TSI IFA-300 anemometer, also used for operating the hot-wire (Sec. II B). The sensor operating temperature was set at 90 °C, yielding an overheat ratio of 1.18. No sensor calibration was performed or applied, and so the raw voltage-output of the CTA bridge was fed directly into the controller. Working with the raw voltage as proxy for the wall-shear stress is justified, given that the control action is binary (controlling an on/off jet) and only involves thresholding around the mean value of the input signal. Moreover, the system identification procedure described in Sec. III B is performed with the raw voltage signal, and it was verified that coherence characteristics are retained even without calibrating the sensor.

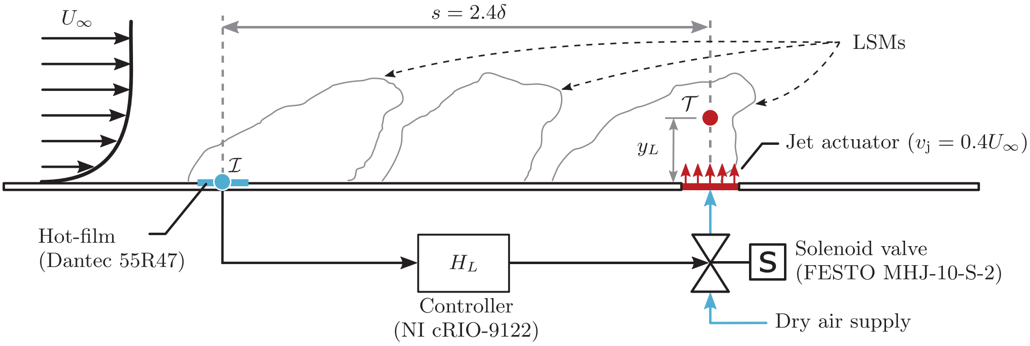

FIG. 3. Schematic of the control system for real-time boundary layer manipulation, integrated in the W-Tunnel facility.

For actuation, a nonzero-net-mass-flux blowing jet is used. Since its exit velocity and frequency response can be tuned with relatively simple adjustments to the hardware, this actuator is ideal for tuning the region of interaction between the jet flow and the grazing crossflow. The development of a jet in crossflow is such that an upwash is created downstream of the injection point as a result of wall-normal momentum injection. Additionally, the steady jet in crossflow creates a counterrotating vortex pair (CVP), originating from the roll-up of the jet plume as the mean shear of the crossflow transfers streamwise momentum to it. Off-centerline, this CVP generates a downwash [41–43]. Note that an investigation of the off-centerline behavior of the boundary layer is not part of the current study; we solely focus on the impact of control directly downstream of the injection point ($z = 0$). The jet flow exhausts in the grazing TBL flow through a rectangular exit slit. Given the requirement of the control system to be persistent downstream, the slit was strongly elongated in the streamwise direction and comprised dimensions of 15 mm × 1.5 mm (in the x and z directions, respectively), or approximately $0.2\delta \times 0.02\delta$. The streamwise elongation of the jet exit slit ensures the formation of a more persistent vortical structure in the streamwise direction, compared to the case when the jet exit is circular in shape [44,45].

Compressed dry air feeds into the actuator, which is operated in an on/off state using an electrically actuated, nominally closed, binary solenoid valve (FESTO MHJ-10-S-2). By way of PIV characterization experiments, described in Appendix A, the frequency response was quantified as well as the jet trajectory into the TBL crossflow as a function of the jet exit velocity. For the frequency response, latency's were inferred from the characterization experiments, and are associated with the time it takes for fluid to accelerate through the pneumatic components ($\tau_{a,1} \approx 3$ ms), for the jet plume to reach the logarithmic region ($\tau_{a,2} \approx 3$ ms), and for the jet to shut-down ($\tau_{a,3} \approx 10$ ms). Even though the solenoid valve has a maximum switching frequency of 1 kHz, the maximum operating frequency for which on- and off-states are reached is lower due to the latency's and equals $f_\mathrm{act} \approx 63$ Hz, given the 6 ms start-up time and 10 ms shut-down time. Concerning the exit velocity, in the final control configuration it was set at $v_\mathrm{j} = 0.4U_\infty$ ($v_\mathrm{j} = 6$ m/s). This ensured that the jet plume remained within the bounds of the logarithmic region for a downstream distance of approximately 1δ. As further elaborated in Appendix A, a lower exit velocity can be beneficial to ensure a lower disturbance on the TBL flow; however, technical limitations of the compressed air supply did not allow operation at lower r.

B. System identification

Both the input sensor and actuator of the control system interact with the grazing flow (see Fig. 3 for a schematic representation of the control system). The streamwise sensor-actuator spacing, s, has important implications given that an increase in s will result in a progressive loss-of-coherence between the turbulence velocities at both stations. Practically, there is a minimum (nonzero) spacing

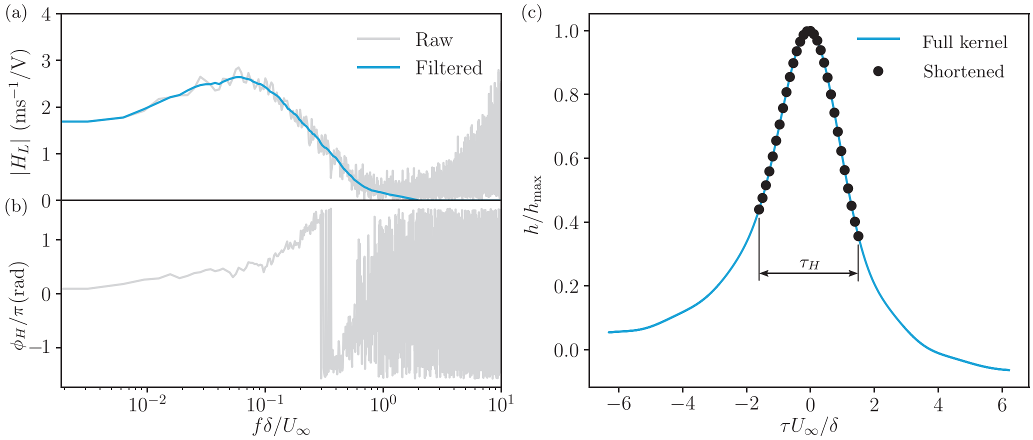

FIG. 4. (a), (b) Bode plot of kernel $H_L(f)$ with the frequency-dependent gain and phase. The gain is shown with both the raw data and a bandwidth-moving filtered version (25% bandwidth). (c) Kernel in physical time, both at the sampling frequency of the calibration experiment (solid line; $f_{\mathrm{HW}} = 51.2\,\mathrm{kHz}$) and at the controller frequency (round markers; $f_{\mathrm{FPGA}} = 2\,\mathrm{kHz}$).

that is realizable for two primary reasons: (1) coherent structures in TBL flow possess an average streamwise inclination angle of 14° to 16° due to the mean shear [28,46]; their footprints are only visible to the wall-based sensor after their signature has passed in the logarithmic region, and (2) input processing introduces latency's in addition to the one of the actuator described earlier. Hence, only with a nonzero distance s it can be guaranteed that there is enough time to act upon LSMs in real-time. To inspect whether a sufficient correlation remains present between sensor and actuator for a nonzero spacing s, a single-input/single-output (SISO) linear time-invariant system analysis was applied as reported in Appendix B. A sufficient level of linear coherence was observed between the input and target locations (points $\mathcal{I}$ and $\mathcal{T}$ in Fig. 3), particularly for a sensor-actuator spacing of $s = 2.4\delta$ that is used in the current study. A motivation for this spacing is presented later on. Given the significant coherence, a linear transfer kernel, H_L, relating the streamwise velocity $u(t)$ in the logarithmic region (the target point) to the voltage signal $e(t)$ of the hot-film (the input point) was determined through an LSE procedure based on data of a control-off experiment (Appendix B). A bode plot of the frequency-dependent kernel $H_L(f)$ is shown in Figs. 4(a) and 4(b). A maximum gain of $|H_L| \approx 2.6\,\mathrm{ms}^{-1}/\mathrm{V}$ occurs at $f\delta/U_\infty \approx 0.06$. The gain decays at higher frequency and is retained up to a cutoff frequency of $f\delta/U_\infty \approx 0.7$, at which the coherence drops below a threshold of $\gamma_L^2 = 0.05$. Beyond this frequency, the scales are incoherent and the kernel's phase becomes random.

Instead of performing an estimation in spectral space following Eq. (B2), the time-domain convolution equivalent is embedded on a real-time controller. The convolutional estimate is $\widehat{u}(t) = (h \circledast e)(t)$, with h being the inverse FFT of the frequency-domain kernel, $h(\tau) = \mathcal{F}^{-1}[H_L(f)]$ [and h thus resembles a finite impulse response (FIR) filter for the input data]. The inverse FFT over the full range of frequencies for generating $h(\tau)$ from $H_L(f)$ yields a kernel in the physical domain with the length of one ensemble size ($N = 2^{17}$, thus $\Delta t_N = 2.56\,\mathrm{s}$). However, given that an FIR convolution in real-time introduces an inherent delay of half the filter-width, the kernel $h(\tau)$ is only retained over a temporal horizon of $\tau_H/2 = 7.5\,\mathrm{ms}$ [centered at the peak-instance of the FIR filter, see the temporal extent of the dotted kernel in Fig. 4(c)]. The shortened kernel length ensures that the sensor-actuator spacing of $s = 2.4\delta$ is attainable in real-time. Note that omitting the tails of the kernel is justified given the negligible contribution to the estimate. Future improvements of a short kernel can be based on the Wiener-Hopf framework so that causality of the kernel is taken into account [47].

Finally, the control loop was implemented on a National Instruments Compact Reconfigurable Input-Output (NI-cRIO-9122) machine with an embedded Field Programmable Gate Array (FPGA) chassis (cRIO-9022). The control logic was implemented in LabVIEW on the FPGA chip with a loop frequency of $f_{\text{FPGA}} = 2\,\text{kHz}$, and FPGA processing was conducted with a 16-bit fixed-point precision. The kernel $h(\tau)$ was down-sampled to the loop frequency of the FPGA controller ($f_{\text{HW}} \rightarrow f_{\text{FPGA}}$). When operating in real-time, the input signal was also sampled at the loop frequency with the aid of an analog-to-digital NI-9234 input module. Trigger commands were provided to the solenoid valve with the aid of a 5V analog signal that was relayed through a NI-9472 digital output module.

C. Control logic definition

For our control problem the actuator interacts with the high- and low-speed LSMs. Based on the input sensor and the pre-identified transfer kernel, the controller is able to estimate the flow state $\widehat{u}$ at the target-point through the convolution mentioned before: $\widehat{u}(t) = (h \circledast e)(t)$. Note that input signal $e(t)$ is a zero-mean signal since the controller only acts upon the fluctuations. The zero-mean signal was obtained in real-time by the subtraction of a converged running mean over a 2 s interval duration [this accounts for a potential drift in the hot-film reading, [48]]. Based on the real-time estimate $\widehat{u}(t)$, high- and low-speed zones are then targeted following a nominal control law:

$$v_{\text{j}}(t) = \begin{cases} 0.4U_\infty, & \text{if } \widehat{u}(t) \geqslant 0, \\ 0, & \text{if } \widehat{u}(t) < 0, \end{cases} \tag{1}$$

with v_{j} being the binary velocity state of the jet actuator. This *opposition* controller will thus only actuate on those large-scale events which are estimated to be more drag-producing than the mean flow. A *reinforcing* controller was also implemented, where the control law was inverted and the actuator targeted a low-speed region instead. To also isolate the effect of operating the jet in a synchronized manner with respect to the incoming LSM structures, versus a desynchronized manner (in essence no real-time control), a *desynchronized* control law was also implemented following Abbassi *et al.* [27]. For the desynchonized control, an on/off signal from the opposition control case was used for actuation, irrespective of the input signal. Given the sensor-actuator spacing s, the control system needs to digitize the analog voltage-input signal, convolve it with the transfer kernel and generate the control-output within the time it takes for the LSM structures to convect to the target point. With $s = 2.4\delta$ ($s = 0.17\,\text{m}$) and $U_c = 9.9\,\text{m/s}$, this duration is $\tau_{\text{conv}} = s/U_c \approx 17.2\,\text{ms}$. The sensor-actuator spacing was chosen based on an analysis of the delays inherent to a real-time controller. First, as mentioned in Sec. III B, the real-time convolution of the input signal with the FIR-like kernel requires half the temporal horizon, thus $\tau_H/2 = 7.5\,\text{ms}$. Additionally, a delay of $\tau_{\text{FPGA}} = 0.5\,\text{ms}$ is added due to the controller looping at $f_{\text{FPGA}} = 2\,\text{kHz}$. As explained in Sec. III A, the actuator itself also introduces two sources of lag: $\tau_{a,1} \approx 3\,\text{ms}$ and $\tau_{a,2} \approx 3\,\text{ms}$. In total, the controller requires the following time for providing an output:

$$\tau_C = \tau_H/2 + \tau_{\text{FPGA}} + \tau_{a,1} + \tau_{a,2} \approx 14\,\text{ms}. \tag{2}$$

Since $\tau_{\text{conv}} > \tau_C$ the sensor-actuator spacing of $s = 2.4\delta$ yields a slightly conservative setup. However, this was deliberately done so that control that would be "too early" could also be investigated. However, for the nominal opposition control mode presented in this paper an extra delay of 7 control loops (i.e., 3.5 ms) was implemented for correct timing of the opposition and reinforcing control modes.

D. Performance evaluation of the state estimation

The state of the boundary layer that the controller actuates upon, $\widehat{u}(t)$, is an estimate. To gauge the performance of the controller, we resort to computing the *binary accuracy* of the estimated state, $\widehat{u}(t)$, that the control actuates upon. Figure 5(a) displays the measured streamwise velocity $u(t)$, as well as the LSE-based estimate simulating real-time conditions. Note that the estimate $\widehat{u}(t)$

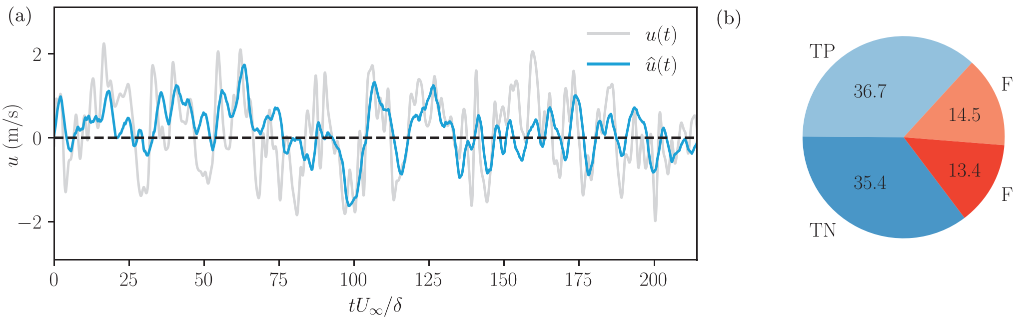

FIG. 5. (a) Sample portion of the measured streamwise velocity $u(t)$, at $x = 0$ and $y = y_L$, compared to the estimated velocity $\widehat{u}(t)$. (b) Pie chart of the binary performance of the estimation, with in blue the true-positive (TP) and true-negative (TN) predictions; in red the false-positive (FP) and false-negative (FN) ones (values are in percentage).

would be shifted by half the kernel's horizon length as a result of the real-time convolution, but this shift is omitted for evaluating the binary accuracy. Since the controller only actuates based upon the estimated signal's sign, it is possible to binarize $u(t)$ and $\widehat{u}(t)$ and compare them directly. At every instant, a true-positive (TP) prediction is made when both signals are positive, whereas both signals being negative will yield a true-negative (TN) prediction. Additionally, false-positive (FP) and false-negative (FN) outputs will occur if $u(t) < 0$ and $\widehat{u}(t) \geqslant 0$, or vice versa, respectively. The binary accuracy (BACC) is then defined as

$$\mathrm{BACC} = \frac{T_{\mathrm{TP}} + T_{\mathrm{TN}}}{T_a}, \tag{3}$$

with the numerator representing the cumulative time that the estimate is true positive (T_{TP}) and true negative (T_{TN}). Note that a BACC of unity does not mean that the $\widehat{u}(t) = u(t)$, but only that $\mathrm{sgn}[\widehat{u}(t)] = \mathrm{sgn}[u(t)]\,\forall\, t$. Figure 5(b) reports the binary performance with BACC equal to 72.1%. This value is significantly larger than 50 % (which would indicate a random process) and justifies the wall-based sensing approach for reactive real-time control. In fact, albeit the imperfect binary accuracy, results in later sections corroborate a statistically correct implementation and targeting of the large-scale structures.

IV. RESPONSE OF THE TURBULENT BOUNDARY LAYER

A. Mean flow and turbulence kinetic energy

Wall-normal profiles of the mean velocity and streamwise TKE (based on the hot-wire profile taken at $x = 2\delta$) aid in explaining the effect of control on the TBL, and allow for a direct comparison to the work of Abbassi *et al.* [27]. Figure 6(a) presents the profiles for both the uncontrolled flow and the opposing, reinforcing and desynchronized control cases. It is evident that only in the logarithmic region a velocity deficit manifests itself for the control cases, in comparison to the uncontrolled flow. This is consistent with the jet injecting momentum in the wall-normal direction, thereby reducing streamwise momentum from the grazing TBL flow [43,49]. At $x = 2\delta$, the jet plume penetrates primarily within the logarithmic region [recall Fig. 17(a) and its discussion], while the mean velocity in the inner region already recovered to the uncontrolled flow condition. Since the jet is activated for the same fraction of time amongst all three control modes (50%), the wall-normal momentum being injected into the boundary layer is equal and thus explains the collapse of the profiles in Fig. 6(a).

Distinctions between the control modes become apparent from the streamwise TKE, $\overline{u^2}$, presented in Fig. 6(b). All profiles collapse in the wake and show that the control influence is confined

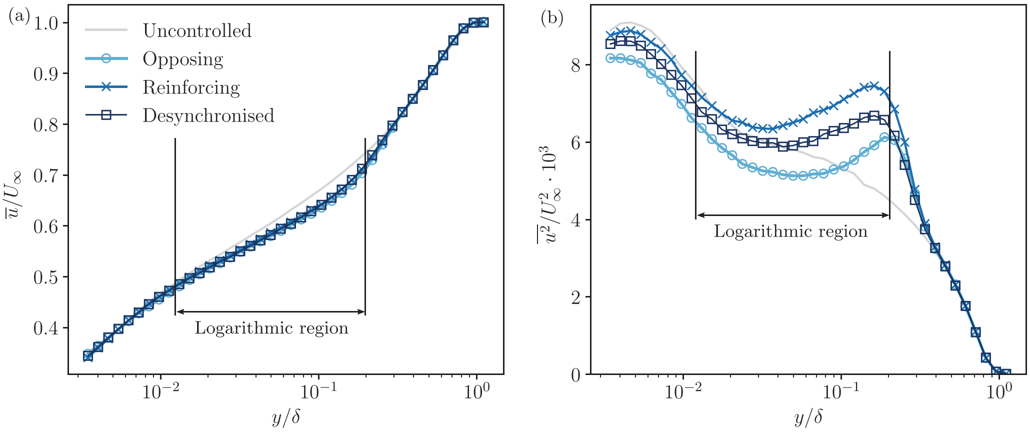

FIG. 6. (a) Wall-normal profiles of mean streamwise velocity, $\overline{u}/U_\infty$, and (b) streamwise TKE, $\overline{u^2}/U_\infty^2$, for the uncontrolled case, as well as for the three control modes, at $x = 2\delta$.

to the inner region. Near the upper edge of the logarithmic region, a hump of $\overline{u^2}$ occurs for all control modes and increases when moving from the opposing, to the desynchronized, and finally to the reinforcing control case. This trend is reflective of the presence of an internal shear layer between the upper side of the jet plume and the grazing TBL flow [42]. The opposing control case lowered the u-variance the most, below $y/\delta \approx 0.1$. This reduction is not only apparent in the logarithmic region but persists down to the wall.

To analyze how the energy across all turbulent scales is changed as a result of control, premultiplied energy spectra are considered in a similar manner as in Fig. 2(b). Figure 7(a) displays the

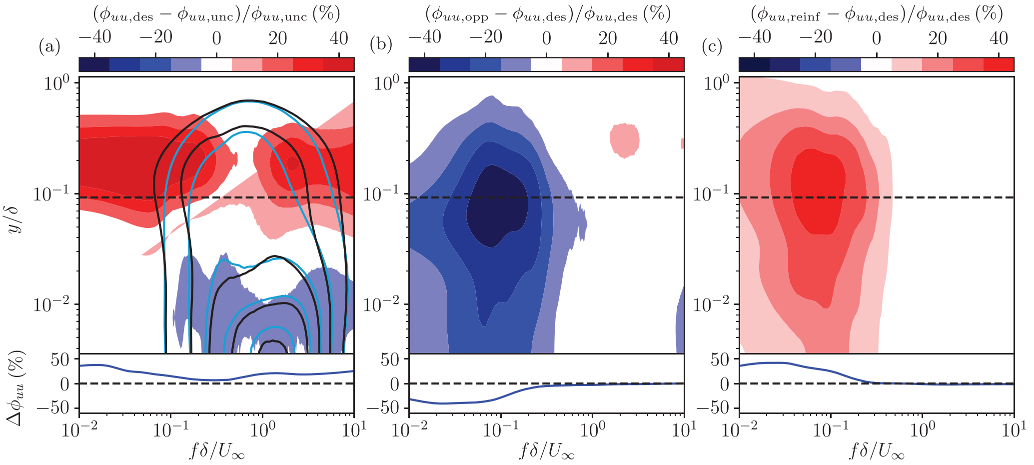

FIG. 7. (a) Filled contours: percentage difference in the premultiplied energy spectrograms of the streamwise velocity, between the TBL affected by desynchronized control and the uncontrolled case. Black contours: spectrogram of the TBL flow subject to desynchronized control (contour levels at 0.4:0.4:2.0). Light blue contours: spectrogram of the uncontrolled TBL flow (contour levels at 0.4:0.4:2.0). (b) Percentage difference spectrograms between the flow subject to opposing control and the desynchronized case. (c) Percentage difference spectrograms between the flow subject to reinforcing control and the desynchronized case. Difference in the energy spectrum at y_L shown below the contour plots in panels (a)–(c) for the corresponding case. All spectrograms were acquired at $x = 2\delta$ and filtered with a bandwidth-moving filter of 25% in width.

spectrogram $f^+\phi^+_{uu,\mathrm{des}}(f, y)$ for the desynchronized case with the black isocontours, overlayed on a filled contour that represents the percentage difference in spectrograms between said case ($\phi_{uu,\mathrm{des}}$) and the uncontrolled flow ($\phi_{uu,\mathrm{unc}}$), following

$$\Delta\phi_{uu} = \frac{\phi_{uu,\mathrm{des}} - \phi_{uu,\mathrm{unc}}}{\phi_{uu,\mathrm{unc}}} \times 100. \tag{4}$$

A region of remarkably higher energy is observed above $y/\delta \approx 0.1$ for all frequencies. This relates to the location where an increase in streamwise TKE was also observed in Fig. 6(b) (note that $\overline{u^2} = \int \phi_{uu} df$). Given the nature of the jet actuator, not only wall-normal momentum is imparted to the flow, but the shear layer developing between the jet plume and the TBL flow enhances turbulent fluctuations. This increase in TKE is thus broadband in nature and is unavoidable with the current type of actuator flow. In fact, actuation by means of unsteady wall-normal momentum injection biases the effect of control towards an increase in energy in the logarithmic region and wake of the TBL, irrespective of the control law. However, this was measured not to have an effect on the absolute skin friction, as will be presented in Sec. V. Below $y/\delta \approx 0.1$, a slight decrease in energy is observed. The superposition effect that the jet actuator was suggested to have in Sec. IV A also appears to be present over a vast frequency band in proximity to the wall ($0.1 < f\delta/U_\infty < 10$). To highlight the changes in spectral energy that the turbulence in the boundary layer undergoes as a result of purely the control logic, and not the actuator-induced flow, reactive control cases are compared to the desynchronized one.

Figures 7(b) and 7(c) present the percentage difference in the spectrograms with respect to the desynchronized control mode for the TBL targeted by opposing and reinforcing control, respectively. An almost perfect symmetry is visible: a region of reduced energy for opposing control is juxtaposed to one of increased energy for the reinforcing control mode, with a maximum effect residing around the geometric center of the logarithmic region at $y^+_L = 3.9\sqrt{\mathrm{Re}_\tau}$ (indicated by the dashed line). A reduction of $\approx 40\,\%$ in ϕ_{uu} in the opposing mode is accompanied by a $\approx 45\,\%$ increase in spectral energy for the reinforcing case. For both modes, the largest change in energy is concentrated at $f\delta/U_\infty < 0.1$, which indicates a successful targeting of the low-frequency (i.e., large wavelength) structures in the logarithmic region. Recall from Sec. III B that the higher-frequencies (smaller-scales) cannot be targeted with the real-time controller due to the absence of input/output coherence at these scales. Energy spectra in the geometric center of the logarithmic region (displayed explicitly in the insets below the contour plots in Fig. 7) furthermore reveal how the percentage difference collapses to zero for $f \gtrsim 0.3U_\infty/\delta$.

B. Conditionally averaged velocity fluctuations

Conditional averages of the streamwise velocity were constructed for examining the local response of the TBL flow. Time series of the streamwise velocity acquired using HWA at all 40 wall-normal locations in the boundary layer were conditioned on the positive-gradient zero-crossings of the estimated velocity signal, $\widehat{u}(t)$, following

$$\widetilde{u}(y,\tau) = \langle u(y,t)\,|\,(\widehat{u}(y,t) = 0 \,\wedge\, \partial\widehat{u}/\partial t(y,t) > 0)\rangle, \tag{5}$$

with τ being the time coordinate of the conditional average and $\tau = 0$ corresponding to the positive-time-gradient zero-crossing. The present work considers the conditional average in a variable time interval (VTI) formulation [50]. Given a signal $\alpha(t)$, we can binarize it to obtain $\overline{\alpha}(t) = 1$ where $\alpha(t) \geqslant 0$ and $\overline{\alpha}(t) = 0$ otherwise. In the context of our work, this signal corresponds to the estimated velocity signal $\widehat{u}(t)$, which is thresholded to create the on/off signal that drives the actuator in real-time. For the VTI analysis, following Eq. (5), we condition the signal $\alpha(t)$ on the rising edges of the binarized signal $\overline{\alpha}(t)$ between the previous and the consecutive falling edges:

$$\widetilde{\alpha}(\tau) = \sum_{i=1}^{N_c} \frac{[\alpha(t)\,|\,(t_{f,i-1} < \tau < t_{f,i})]}{N_c}, \tag{6}$$

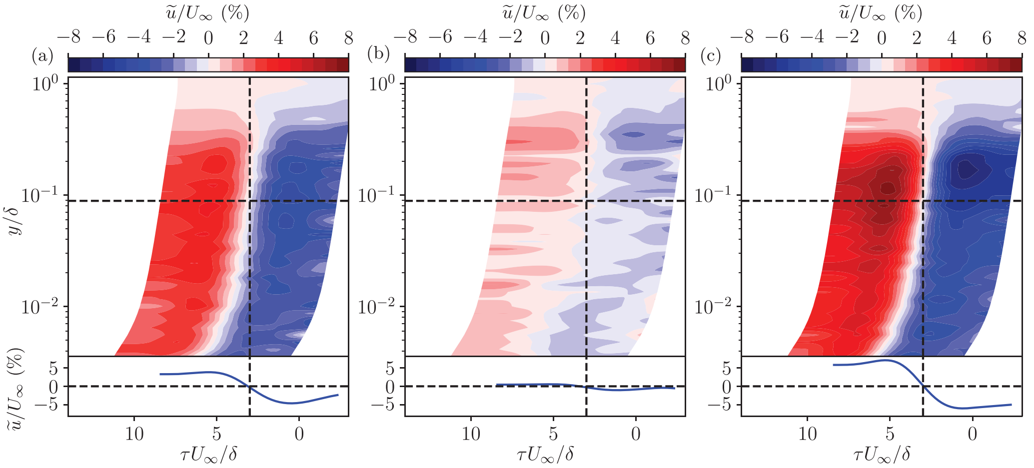

FIG. 8. Conditionally averaged response, $\widetilde{u}/U_\infty(y,\tau)$, of the streamwise velocity, conditioned on the zero-crossing positive-time-gradient of the estimated signal $\widehat{u}(t)$. Detail of response at y_L shown below the filled contour plot. (a) Uncontrolled flow, (b) opposing, and (c) reinforcing control modes.

with N_c being the total number of conditioning points (i.e., the total number of averaged signal samples), $t_{f,i}$ is the time instant corresponding to the falling edge in $\overline{\alpha}(t)$ following the conditioning rising edge and $t_{f,i-1}$ the instant corresponding to the preceding falling edge.

The conditionally averaged velocity contour, $\widetilde{u}(y,\tau)/U_\infty$, is shown in Fig. 8 for the uncontrolled, opposing and reinforcing control cases. The time coordinate τ is nondimensionalized using the factor U_∞/δ, making it representative of the nondimensional distance from the streamwise position of the actuator to the downstream position of the hot-wire probe ($x = 2\delta$). Thus, the zero-crossing occurs at $\tau U_\infty/\delta = (2\delta/U_c)U_\infty/\delta \approx 3$ [remember $U_c = \overline{u}(y_L^+ \approx 190)$ is the convection velocity in the logarithmic region]. In the contour representation a total time-interval of $\Delta\tau U_\infty/\delta \approx 11.2$ is preserved around the conditioning point. When the convection velocity reduces, such as at locations close to the wall, the time needed for the response to be measured is longer. Hence, the time-instant of the zero-crossing in $\widetilde{u}(y,\tau)$ gradually shifts towards increasing values of τ when approaching the wall.

The uncontrolled case in Fig. 8(a) reports the baseline velocity fluctuations the controller will actuate upon. The effect of control becomes apparent in the conditional averages for the opposing and reinforcing cases. The former causes an overall reduction of more than 60 % in the amplitude of the oscillation observed in the uncontrolled case, while the latter clearly amplifies it by approximately 60%. This effect is particularly visible in the bottom insets, showing the conditionally averaged time series at y_L. Residing back to the wall-normal TKE profiles presented in Fig. 6(b), an increase in TKE in the logarithmic region and in the wake of the TBL was noticeable when control is active. However, this is accompanied in the conditional average with still a reduction in the amplitude of $\widetilde{u}$ as seen in Fig. 8. This can be explained as follows: the spectrograms in Fig. 7 revealed a *broadband* increase in energy in the wake of the TBL. Since the controller only detects and acts upon large-scale velocity structures, with frequencies lower than $f\delta/U_\infty \lesssim 0.3$, conditional averaging on the velocity fluctuations targeted by control inherently averages-out the small-scale fluctuations.

Conditional averages of velocity fluctuations as shown in Fig. 8 only report the fluctuations in streamwise velocity as a result of control, but fail to capture the global interaction of the actuator flow with the grazing TBL flow. This void can be filled by utilizing PIV velocity fields, which are here presented for a domain with dimensions of roughly $1.8\delta \times 0.8\delta$ (half of the FOV listed in the bottom line of Table I). Processing was performed with the aid of LaVision DaVis 10.2 utilizing a multi-pass approach, leading to a final vector resolution of 2.25 vectors/mm. The acquisition was

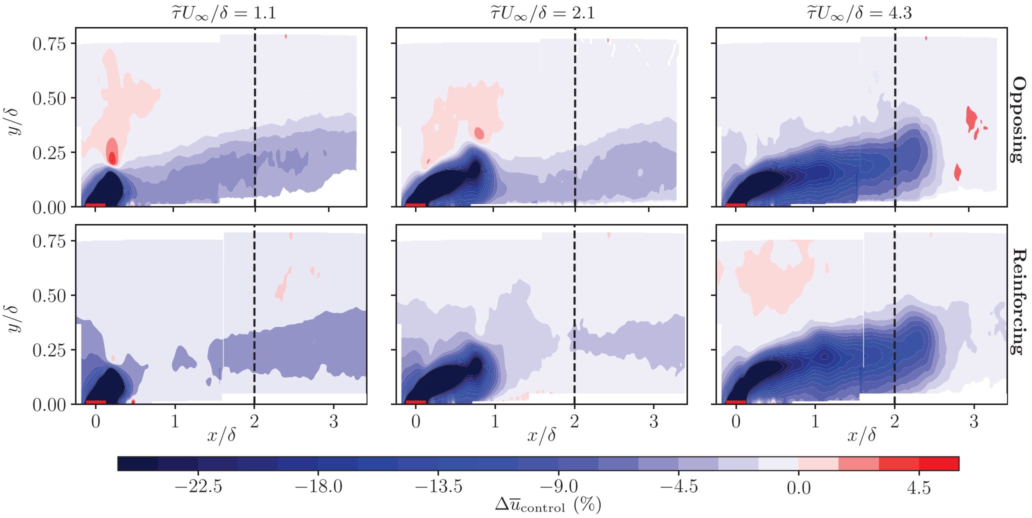

FIG. 9. Phase-averaged field of the percentage variation of mean streamwise velocity component $\overline{u}$ for opposing (top row) and reinforcing (bottom row) control modes with respect to the uncontrolled flow. Phase-averaged acquisition acquired at $\tilde{\tau}U_\infty/\delta = 1.1$, $\tilde{\tau}U_\infty/\delta = 2.1$, and $\tilde{\tau}U_\infty/\delta = 4.3$. All fields were filtered with a Gaussian filter having a kernel width of $0.25\delta \times 0.25\delta$ and $\sigma = 0.1\delta$. Dashed lines indicate the position of the hot-wire profile. Shown in red is the position of the jet exit slit.

synchronized to the controller and was triggered with a specified delay, relative to the instance of an actuator on-command. This was repeated for a sequence of delays, allowing a visualization of the jet plume entering into the grazing TBL flow. The fields shown in Fig. 9 display the percentage variation of the streamwise velocity component, $\Delta\overline{u}_{\text{control}} = (\overline{u}_{\text{control}}/\overline{u}_{\text{unc}} - 1) \times 100$ (%), with respect to the uncontrolled flow for three temporal delays, $\tilde{\tau}$. Results for the opposing control mode are shown in the top row, whereas the results corresponding to the reinforcing strategy are shown in the bottom one. The low-velocity (blue) region on the bottom of each contour plot corresponds to the jet plume entering the domain. At an early stage ($\tilde{\tau}U_\infty/\delta = 1.1$, or $\tilde{\tau} = 5$ ms), a higher-than-average velocity is observed for the opposing case, which also persists at $\tilde{\tau}U_\infty/\delta = 2.1$ ($\tilde{\tau} = 10$ ms), suggesting that the controller successfully targets high-speed events. The opposite condition is, instead, measured in the reinforcing control scenario, where the controller is observed to intervene on low-speed events rather than high-speed ones. When time elapses to $\tilde{\tau}U_\infty/\delta = 4.3$ ($\tilde{\tau} = 20$ ms), the conditional flow field evolves to a condition where lower and higher streamwise velocity above the actuator are observed for the opposing and reinforcing cases, respectively.

V. EFFECT OF CONTROL ON TURBULENT SKIN-FRICTION DRAG

Our principal goal is to investigate the change in turbulent skin-friction drag in relation to a control logic that specifically targets drag-producing large-scale structures. While any wall-normal jet actuator causes reductions in wall-shear stress, which can even lead to flow separation in the near-field of the actuator for elevated momentum coefficients, the goal of this section is to illustrate the benefits of performing *timely* actuation to attenuate high-momentum large-scale events.

The dimensional form of the wall-shear stress, $\tau_w = \mu \partial\overline{u}/\partial y|_{y=0}$, is analysed in terms of the skin-friction coefficient,

$$C_f = \frac{\tau_w}{q_\infty} = 2\frac{U_\tau^2}{U_\infty^2}. \tag{7}$$

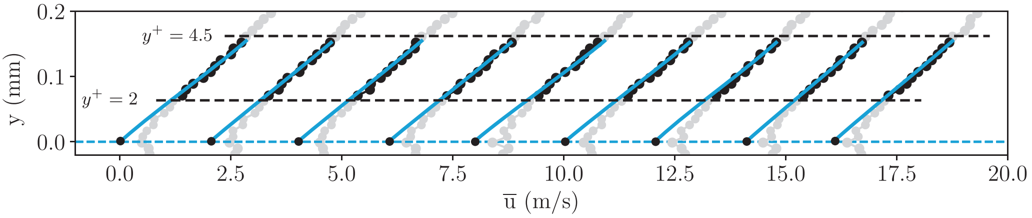

FIG. 10. PTV-based profiles of the streamwise velocity $\overline{u}$ with increasing wall-normal distance y for the uncontrolled flow at the FOV centered at $x/\delta = 2.0$. Profiles are sequentially separated in the horizontal direction by $\Delta\overline{u} = 2\,\mathrm{m/s}$ for ease of inspection.

Here, $q_\infty = \rho_\infty U_\infty^2/2$ is the freestream dynamic pressure. Due to heat transfer effects from a hot-wire to the tunnel's surface, the HWA technique cannot reliably capture the velocity in the linear region [51,52]. As such, traditional estimates of C_f from hot-wire measurements typically rely on boundary layer scaling laws and mathematical fits to the streamwise velocity profile (e.g., the composite fit [37] or the well-known Clauser fit procedures). With a boundary layer strongly affected by control and additional momentum injection from the jet actuator, the assumptions behind these methods are violated. Therefore, a direct measurement of the velocity gradient at the wall, based on PTV, is pursued in our current work.

A. Skin-friction determination from PTV

The PTV technique was applied to a relatively small FOV of size $0.33\delta \times 0.28\delta$ (recall Table I). The acquisition was not time-resolved, thus all PTV tracks consist of only two points. A PTV-based approach was implemented with an unparalleled resolution of velocity vectors over a PIV-based technique. With the given pixel resolution and typical interrogation window sizes, only very few valid vectors would be obtained from PIV in the linear region ($y^+ < 5$) for our Reynolds number of $\mathrm{Re}_\tau \approx 2\,240$. Given the linear dependence $\overline{u}^+ = y^+$ for the velocity profile in this region, only two measurement points would theoretically be required to compute the gradient, $\partial\overline{u}/\partial y$. However, more information is required to increase the robustness of the measurement-based estimation due to stochastic noise and uncertainty. The following six post-processing steps were implemented to infer the skin-friction data from the raw images.

(1) *Particle track computation.* 2D Lagrangian particle tracks are computed with the aid of LaVision DaVis, version 10.2. Only a small subset of the original FOV is retained, that encompasses the wall and a small region above and below it ($\Delta y = 0.05\delta$ and the full streamwise extent).

(2) *Wall identification.* Reflections of the particles in the flow result in mirrored particle tracks "below" the wall. This reflection allows for a precise identification of the wall. The ensemble-averaged mean velocity field is computed through traditional PIV processing on a subset of image pairs (500 of the 2 000 in total), after which the wall position is found by utilizing the wall-mirrored field [53,54]. That is, a parabola fitted to points in the linear region (both above and below the reflection line) yields $\overline{u} = f(y)$. Its minimum velocity point is taken to be the y-position of the wall, denoted as y_w. This procedure is performed over 330 streamwise positions spanning the entire FOV (corresponding to the vector spacing of the coarse PIV processing), resulting in a functional form for the wall position, $y_w(x)$.

(3) *Particle track correction.* Each y coordinate from the particle tracks found in step 1 is corrected to account for the true wall-position. This correction is based on each x position of the particle track, for which the wall position $y_w(x)$ is known. After this correction, the wall-normal profiles of $\overline{u}$ are symmetric around $y = 0$, as seen in Fig. 10.

(4) *Binning definition.* All corrected tracks are binned spatially. Streamwise-elongated bins of size $128 \times 1\ \mathrm{pix}^2$ are initialized. Given the pixel resolution of the images, this equates to a size of $1.08 \times 0.008\,\mathrm{mm}^2$ ($34.7l^* \times 0.27l^*$). Note that the FOV spans 20 bins in x (given the 2 650 pixels

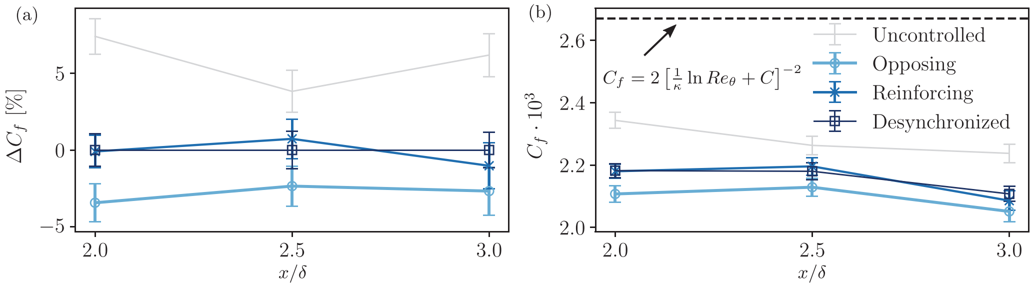

FIG. 11. (a) Percentage difference between the skin-friction coefficients of uncontrolled, opposing and reinforcing cases with respect to the desynchronized one with error bars showing the uncertainty. (b) Absolute skin-friction coefficient for the four control modes with error bars showing the uncertainty. Dashed line plotted for the value of C_f estimated from the Coles-Fernholz relation.

in the streamwise direction, and the 128 pixel bin size). The degree of elongation is only feasible if the wall is parallel to the major axis of the bin, which was ensured through steps 2 and 3.

(5) *Binning procedure.* Each individual particle track is collected in the bins defined in step 4 according to the coordinates of their midpoints.

(6) *Velocity profile generation.* Particle tracks in each bin are averaged to compute the mean streamwise velocity per bin. Knowing the vertical bin spacing, the gradient $\partial\overline{u}/\partial y$ can be determined to infer C_f.

The higher the number of particle tracks, the more statistically reliable the estimation of the mean C_f becomes. A convergence analysis was performed by considering one single bin at $y^+ \approx 15$, where the highest fluctuations in streamwise velocity fluctuations occur. For convergence of the mean streamwise velocity $\overline{u}$, it was found that at least 1 500 image pairs are required for an estimate within 0.8 % of its final value (determined from all 2 000 image pairs).

For each of the vertical profiles (each corresponding to one column of bins), 18 velocity vectors reside within the range $y^+ < 5$. Figure 10 displays 9 wall-normal profiles of $\overline{u}$. The (corrected) wall is positioned at $y = 0$ and is shown with the blue dashed line. Due to some noise in the particle images in proximity to the wall, the points that were selected for determining the gradient $\partial\overline{u}/\partial y$ were within the range $2 < y^+ < 4.5$ (a buffer of $0.5l^*$ is taken between the linear and the buffer regions). This results in 11 points (black markers in Fig. 10) being available for fitting the linear relation, shown in light blue. To enforce the no-slip condition at the wall, the fitting procedure also includes the constraint $(\overline{u}, y) = (0, 0)$. The final value of the wall-shear stress is taken as the average of the individual gradients computed from each of the 20 wall-normal profiles in one FOV, thus assuming streamwise-invariance.

The procedure thus far allows for an estimation of C_f for each FOV of the PTV campaign and thus for the three FOV's centered at $x/\delta = \{2, 2.5, 3\}$ [recall Fig. 1(c)]. At the same time, four control modes are considered (uncontrolled flow, and desynchronized, opposing and reinforcing control). Figure 11(a) displays the percentage difference between the C_f of the desynchronized case and the one of the other three cases [thus $\Delta C_f = 100(C_{f,i} - C_{f,\mathrm{des}})/C_{f,\mathrm{des}}$, with i being the control mode in consideration and $C_{f,\mathrm{des}}$ corresponds to the desynchronized case]. The choice of the desynchronized control as the reference case follows the same reasoning as was followed in presenting the spectrograms in Sec. IV A. Opposing control shows a reduction of 7-11 % in C_f, whereas the reinforcing case reduces friction by 3–7%, depending on the streamwise location. All control modes appear to reduce friction drag with respect to the uncontrolled flow, which is mainly the consequence of the jet injecting wall-normal momentum, which reduces the streamwise momentum of the grazing TBL flow. Reinforcing control has a comparable effect on the TBL to the desynchronized mode in this regard, but it is evident that the opposing mode reduces C_f by 2–3% for all streamwise locations.

Figure 11(b) displays the absolute skin-friction coefficient. The displayed error bars were computed by assuming that each vertical profile of the streamwise velocity from binned PTV tracks generates a statistically independent result, and thus indicate the estimation uncertainty. This uncertainty can be attributed to two main factors: (1) the uncertainty in the convergence of the average streamwise velocity from the PTV measurements, and (2) the uncertainty in the linear fitting procedure described earlier. The former can be computed by considering the number of tracks in each bin and can be defined as $\varepsilon = \sigma_u/\sqrt{N_t}$, where σ_u is the standard deviation of the streamwise velocity samples in the considered bin and N_t the number of tracks. The latter source of error stems from the linear fitting procedure at each streamwise location and is defined as the average RMS residual across all fitted curves.

The skin friction found from the empirical Coles-Fernholz relation ($C_f = 2[\frac{1}{\kappa}\ln \mathrm{Re}_\theta + C]^{-2}$, with $\kappa = 0.38$, $C = 3.7$ and $\mathrm{Re}_\theta = 6\,830$) is also plotted in Fig. 11(b). Our uncontrolled flow experiment yields a C_f that is roughly 15% lower than the one found with the skin-friction determination. This discrepancy is minor, given that the empirical Coles-Fernholz relation is valid for fully developed and smooth-wall TBL flow. Our experiment may include a residual signature from the upstream trip [55] and the jet exit slit embedded within the wall. As such, our uncontrolled and desynchronized cases serve as baseline scenarios.

B. Turbulent skin-friction integrals

Direct assessments of skin friction do not capture the mechanisms behind skin-friction generation. Analysis of PIV data on a larger field of view allows for the computation of TBL integral measures, and to relate them to the changes in skin friction for different control modes. We thus extend the work of Abbassi *et al.* [27], in an attempt to shed more light on the effect of the different control modes on the main skin-friction-generating mechanisms. At first, the TKE production term is informative for investigating the relation between the mean C_f and fluctuations of velocity. TKE production is defined as the product of the Reynolds stress component $R_{xy} = \overline{u'v'}$ and the wall-normal gradient of $\overline{u}$ [56]:

$$P(y) = -\overline{u'v'}\frac{\partial \overline{u}}{\partial y}. \tag{8}$$

A bulk TKE production following $\widetilde{P} = \int P(y)dy$ is an indicator of the total turbulent shear stress within the TBL flow [32,57]. Essential to the computation of P is the Reynolds shear stress R_{xy}, of which a comparison is shown in Fig. 12, for the uncontrolled and the desynchronized control cases. While for the uncontrolled case the Reynolds stress monotonically decreases with increasing y (and resembles a streamwise invariant behavior), the desynchronized case is associated with a band of high-magnitude R_{xy} around $y/\delta \approx 0.35$ at $x/\delta = 2$. A large increase in the magnitude of R_{xy} occurs where the jet enters the domain. As the plume develops into the mid-to-far field of the jet actuator, given the relatively low velocity ratio, the plume resembles a concatenation of hairpin vortices, which eventually rise and break up [42], creating an internal shear layer and, thus, an increase in turbulent fluctuations. The signature of high R_{xy} magnitude persists to the downstream end of the FOV in Fig. 12(b).

To continue a more quantitative assessment, we first consider the TKE production term at a single streamwise location ($x = 2\delta$). Further on we extend this to all streamwise locations captured by the PIV data in Fig. 12. So for $x = 2\delta$, Fig. 13(a) displays the premultiplied TKE production term as a function of wall-normal distance, for the four control modes. Streamwise averaging over a width of 0.2δ in the interval $1.9 < x/\delta < 2.1$ was performed to attenuate measurement noise. The production curve for the uncontrolled case rises to a maximum around $y/\delta \approx 0.01$, before plateauing in the logarithmic region and further decreasing into the wake; this is consistent with the literature [56,57]. The TKE production curves for all other cases show a lower magnitude, up to $y/\delta \approx 0.2$. The region of strong R_{xy} on the upper side of the jet flow-trajectory [seen in Fig. 12(b)] is responsible for the drastic increase in P. To assess changes in the bulk TKE production, integrals of the curves

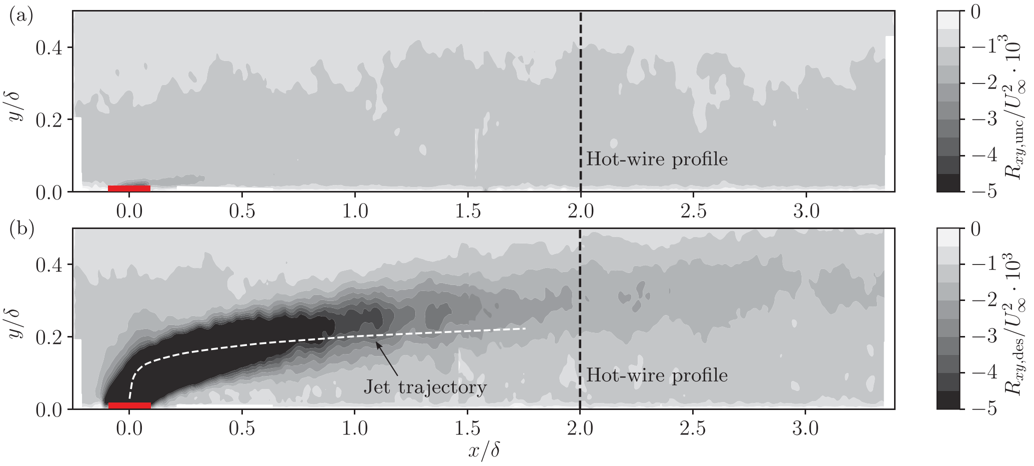

FIG. 12. Contours of the Reynolds stress R_{xy} obtained from PIV data for (a) the uncontrolled flow, and (b) the desynchronized control case; the jet trajectory is duplicated from Fig. 17(a). Shown in red is the position of the jet exit slit.

shown in Fig. 13(a) are considered. Here, the integration is split into two different domains. A first contribution comes from integrating the profiles from the lowest y location up to $y/\delta = 0.2$, where the control cases show a decrease in TKE production. A second contribution comes from the part of the curve at $y/\delta > 0.2$, up to the upper edge of the FOV near $y/\delta \approx 0.8$. Figure 13(b) displays the two portions of the bulk TKE production as a percentage change with respect to the uncontrolled flow. The first integral shows a trend that resembles the behavior observed in Fig. 11. Namely, the uncontrolled case shows the highest value, followed by reinforcing, desynchronized and opposing control modes. The integral in the outer region of the boundary layer contributes up to $\approx 30\%$ to the total integral value, $\widetilde{P}$, in the uncontrolled case. For the flow subject to control, this shows a drastic increase of the control modes' production term with respect to the uncontrolled flow, which is again ascribed to the region of strong R_{xy} in Fig. 12(b). This drastic increase in off-diagonal Reynolds stresses is purely related to the development of a shear layer between the main jet plume and TBL

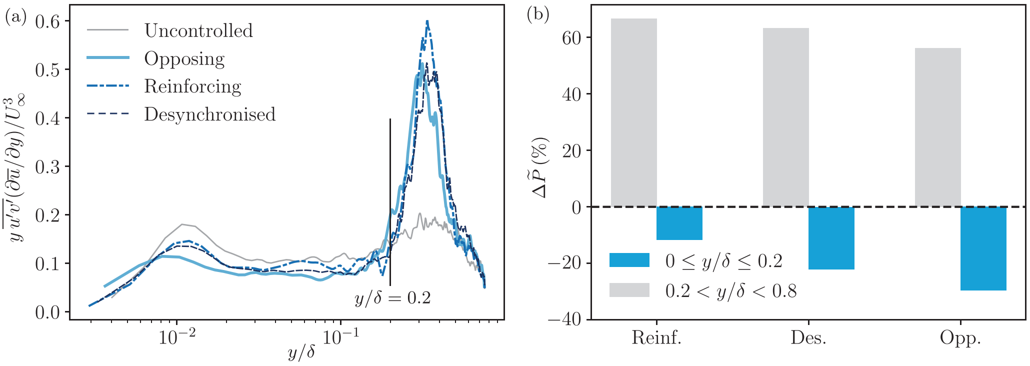

FIG. 13. (a) Plot of normalized, premultiplied TKE production $yP = y\,\overline{u'v'}(\partial\overline{u}/\partial y)/U_\infty^3$, as a function of wall-normal distance at $x = 2\delta$ and the four control modes. Wall-normal profiles of P were computed by averaging PIV data in the streamwise direction in the interval $1.9 < x/\delta < 2.1$. (b) Bar chart displaying the percentage difference of the integrated TKE production term with respect to the uncontrolled flow, for $0 \leqslant y/\delta \leqslant 0.2$ (blue) and for $0.2 < y/\delta \leqslant 0.8$ (gray bars).

crossflow and does not alter the principal working mechanism of the opposition control logic, as can also be observed from direct skin-friction measurements (see Fig. 11).

Fukagata *et al.* [33] derived the so-called *FIK identity* to decompose the flow contributions to turbulent skin-friction coefficient into three components, each of which is responsible for a different mechanism of skin-friction generation [33,58]. The first component ($C_{f,1}$, Eq. 9a) is dependent on the displacement thickness of the boundary layer and is known as the "laminar component". For a TBL flow, $C_{f,1}$ only accounts for a marginal fraction of the total friction coefficient (about 1.4% in the present study). The second component ($C_{f,2}$, Eq. 9b) is related to turbulence fluctuations generating wall-shear and is dependent on the off-diagonal Reynolds stress. Finally, the last component accounts for the spatial and temporal development of the flow [$C_{f,3}$, Eq. (9c)] and is relatively small for a fully developed TBL [32]. For the current analysis, given long-time average statistics, the temporal term $\partial\overline{u}/\partial t$ can be neglected:

$$C_{f,1} = \frac{4(1-\delta^*/\delta)}{\mathrm{Re}_\delta}, \tag{9a}$$

$$C_{f,2} = \int_0^1 \underbrace{-\frac{4}{U_\infty^2}\left[\overline{u'v'}\left(1-\frac{y}{\delta}\right)\right]}_{=f_2(y)} d\left(\frac{y}{\delta}\right), \tag{9b}$$

$$C_{f,3} = \int_0^1 \underbrace{-2(1-y/\delta)^2\left[\overset{\approx 0}{\cancel{\frac{\partial\overline{u}}{\partial t}}} + \frac{\partial\overline{u}^2}{\partial x} + \frac{\partial(\overline{u}\,\overline{v})}{\partial y}\right]}_{=f_3(y)} d\left(\frac{y}{\delta}\right). \tag{9c}$$

In must be stressed here that a few assumptions underlying the formulation of the FIK identity are not met in the present work. Namely, the controlled TBL is not in a canonical state (especially in the region close to the actuator) and the flow is spanwise inhomogeneous. However, given the complexity in performing direct skin-friction measurements and the strong relation that exists between the principal term of the FIK identity, $C_{f,2}$, and drag-producing mechanisms, it is still explored as a metric in evaluating the change in flow physics as a result of control on the TBL and validating the drag-reducing trend inferred with direct C_f measurements.

The integrand of $C_{f,2}$ [$f_2(y)$ in Eq. (9b)] vaguely resembles the premultiplied TKE production term, where R_{xy} is scaled with the wall-normal coordinate. However, the former scales directly with y, while the latter scales with $1 - y/\delta$, thus being multiplied by a factor that decreases with wall-normal distance. Figure 14(a) displays the integrand of $C_{f,2}$ as a function of y/δ and the four control modes. A steady rise is observed up to $y/\delta \approx 0.01$, followed by a plateauing region. In the wake of the boundary layer, again a sharp peak is reminiscent of the enhanced Reynolds shear stress caused by the jet plume. Figure 14(b) shows Eq. (9b) split up in two contributions: again, up to $y/\delta = 0.2$ (blue) and from 0.2 to the edge of the FOV (gray). Also for this metric, the observation can be made that the opposing control law is the most effective in lessening shear stress (at least when integrated up to the $y/\delta = 0.2$).

The analysis of turbulent skin-friction drag integrals assists in identifying where important mechanisms occur within the TBL that contribute to the generation of skin-friction drag. Both the integrated TKE production (Fig. 13) and $C_{f,2}$ (Fig. 14) reveal how the spatiotemporal dynamics of the TBL are altered as a function of y. The full integrals over the available wall-normal range suggest an increase in skin-friction drag, but this contradicts the measured skin-friction coefficients presented in Sec. V A. This discrepancy can be explained by analyzing the trends of the curves in the wake of the TBL flow. By inspection of the TKE profiles in Fig. 6(b), as a well of the distribution of R_{xy} in Fig. 12(b), it is evident how the jet plume created by the actuator is responsible for this sudden rise. Instabilities induced by the break-up of the shear layer of the jet in the TBL are superimposed on top of the naturally occurring Reynolds stresses, thus biasing the integral values of $\widetilde{P}$ and $C_{f,2}$.

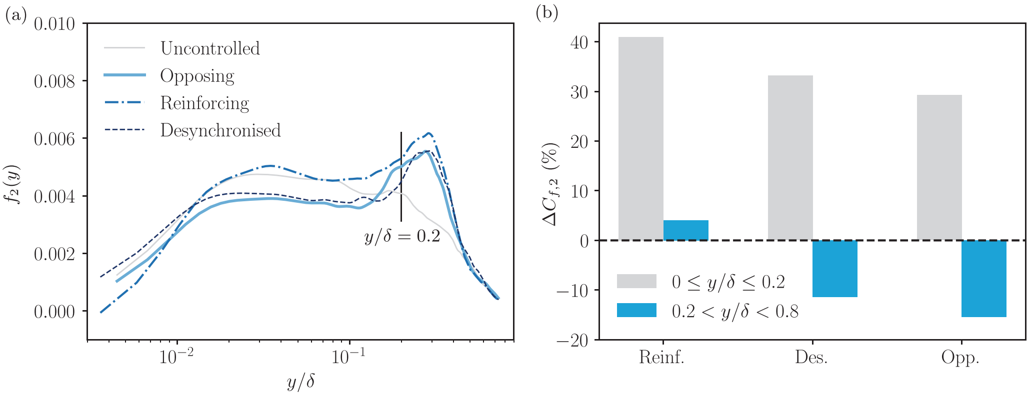

FIG. 14. (a) Integrand of the $C_{f,2}$ expression of Eq. (9b) as a function of wall-normal distance, for $x = 2\delta$ and the four control modes. (b) Bar chart displaying the percentage difference of the integrated $\partial C_{f,2}/\partial y$ term with respect to the uncontrolled flow, for $0 \leqslant y/\delta \leqslant 0.2$ (blue bars) and for $0.2 < y/\delta \leqslant 0.8$ (gray bars).

Still, the reduction in the integrand curves observed in the logarithmic region and below show that the main wall-shear producing dynamics are, in fact, suppressed below the wall-normal coordinate where R_{xy} suddenly rises.

The integrand of $C_{f,3}$ [$f_2(y)$ in Eq. (9c)] is presented in Fig. 15(a) at $x = 2\delta$ and shows a rather low and constant value, especially when compared to the dominant (second) component, as illustrated in the bar chart in Fig. 15(b). Here, the relative contributions of the three components of skin friction are presented for the uncontrolled case as well as the three control modes, in comparison to the friction coefficient components obtained for the uncontrolled flow. For the latter, the magnitude of the relative contributions of the three components of skin friction to the total wall-shear is in accordance with the results of Deck *et al.* [32] at $\mathrm{Re}_\theta = 7\,000$. For the three active control modes, it is evident that the dominant contributing component is $C_{f,2}$ at $y/\delta > 0.2$, which is greatly increased by the actuator-induced internal shear layer.

While Figs. 13–15 present an analysis of the turbulence integral quantity at one streamwise location of $x/\delta = 2$, Fig. 16 illustrates the streamwise variation of the same integral quantities over

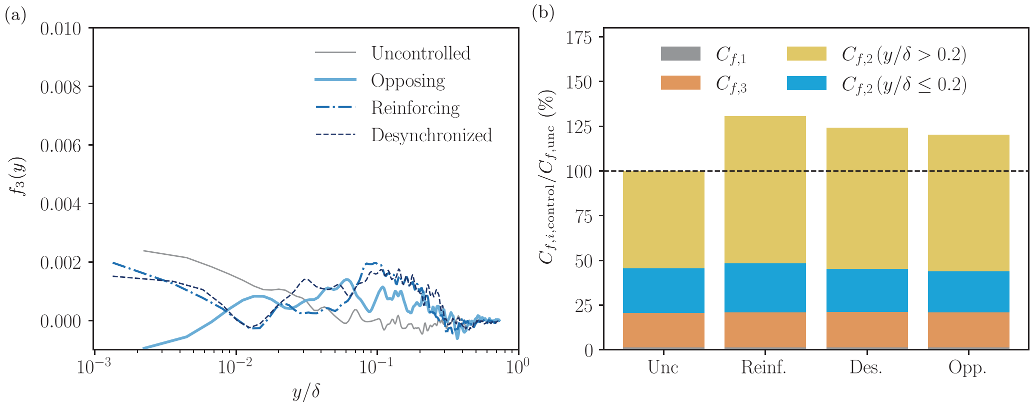

FIG. 15. (a) Integrand of the $C_{f,3}$ expression of Eq. (9c) as a function of wall-normal distance, for $x = 2\delta$ and the four control modes. (b) Bar chart displaying the relative contribution to the total skin-friction coefficient of each of the three FIK-components for the four control modes. A further subdivision of $C_{f,2}$ is made to report contributions from different regions in wall-normal direction.

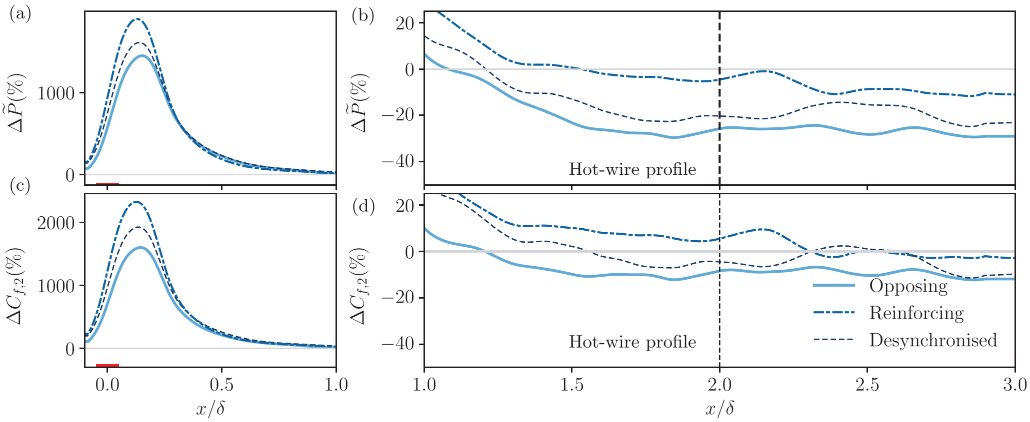

FIG. 16. (a), (b) Streamwise percentage variation in turbulence kinetic energy integrated in the region $0 < y/\delta \leqslant 0.2$ for the three cases influenced by control with respect to the uncontrolled flow. Shown for (a) $-0.1 \leqslant x/\delta \leqslant 1$ and (b) for $1 < x/\delta \leqslant 3$. (c, d) Streamwise percentage variation in $C_{f,2}$ integrated in the region $0 < y/\delta \leqslant 0.2$ for the three cases influenced by control with respect to the uncontrolled flow. Shown for (c) $-0.1 \leqslant x/\delta \leqslant 1$ and (d) for $1 < x/\delta \leqslant 3$.

the whole domain captured by the PIV acquisitions. As it was the case for the above-mentioned figures, integration was performed on streamwise-averaged wall-normal profiles having a width of 0.2δ. Figures 16(a) and 16(c) display the streamwise variation of the integral quantities in the vicinity of the jet actuator ($-0.1 \leqslant x/\delta \leqslant 1$). Given the dominant presence of the jet exit plume developing through the inner region of the TBL in the considered part of the domain, strong spatial gradients are hereby induced, which result in the local integral attaining extreme values. Figures 16(b) and 16(d), however, report the same variation in a region of the fluid domain where the streamwise development of the jet plume has tapered off. Here, the trend that was already discussed in Figs. 13 and 14 is evident for a much larger streamwise extent. The opposing control scheme causes the most reduction in both $\widetilde{P}$ and $C_{f,2}$, with reinforcing control instead causing either an increase or no change in either metric. Given that direct skin-friction measurements are characterized by a relatively high uncertainty, this trend consistency also serves as validation to the direct inference procedure.

VI. CONCLUSIONS AND OUTLOOK

Successful experimental real-time targeting of large-scale motions has been accomplished by means of a control system comprising a surface-mounted hot-film as the input sensor and a wall-embedded blowing jet actuator, located downstream of the sensing element. An opposition control logic was implemented for which the controller activated the actuator at regions of streamwise momentum surplus. The inverse control law, reinforcing control, was also implemented, where the jet fired into regions of momentum deficit with the goal of enhancing turbulence instead of suppressing it.

The response of the TBL to control in terms of first-order velocity statistics follows an expected trend as a result of wall-normal momentum injection imparted by the actuator, with the mean velocity profile experiencing a downward shift when control is applied with respect to uncontrolled flow conditions. Additionally, the inner peak observed in the velocity variance decreases in intensity by $\approx$12%. The analysis of energy spectrograms of streamwise velocity reveals that, for the opposing and reinforcing control cases, a reduction of 40% and an increase of 50% in energy, respectively, occur in the geometric center of the logarithmic region with respect to desynchronized control. The skin-friction coefficient was directly inferred from PTV measurements. It is observed that all control modes in consideration cause a reduction in turbulent skin friction, with opposing control reducing skin friction by 2–3% with respect to the desynchronized, and by 7–11% with respect to the uncontrolled case.

The principal objective of this work was to analyze skin-friction-drag-generating mechanisms by considering statistical integral measures. The bulk turbulence kinetic energy production term decreases up to a wall-normal location where the actuator-induced fluctuations are strong. The sharp increase in the Reynolds shear stresses R_{xy} induces a bias in this integral measure as well as the second component of skin friction following FIK-decomposition: $C_{f,2}$. The applicability of the FIK decomposition relies on the assumption of zero-pressure-gradient fully developed turbulence, which might be violated in proximity to sites where flow control is performed by means of fluidic actuators. However, when focusing on the region downstream of the actuator ($x/\delta > 1$), the Reynolds shear-stresses show streamwise-invariant behavior in the logarithmic region, where the LSMs were targeted. When evaluating $C_{f,2}$ in this region, an identical trend in the change of the skin friction was found as compared to the direct PTV-based measurements. This opens up an avenue for using off-the-wall flow field information downstream of control for the purpose of optimizing a drag-reducing control scheme. Still, the observation that statistical integrands directly reflect changes in PTV-inferred skin-friction coefficient supports the conclusion that the controller presented in this work is able to alter skin-friction-generating mechanisms not only in the logarithmic region, but also in the near-wall region, where small viscous scales are energetically dominant.

To conclude, this study explored the relation of an opposition control law acting on large-scale motions in a turbulent boundary layer, to the skin-friction-producing mechanisms. Further work by is being carried out on developing a multiple-input multiple-output (MIMO) system that acts not only on temporal information at a single spatial location, but at a multitude of spatial locations based on spanwise, wall-based input data. This strategy is expected to increase the spatial domain of influence and the accuracy of the controller (through a closed-loop architecture and adaptive control).

ACKNOWLEDGMENTS

We gratefully acknowledge the Department of Flow Physics & Technology of the Faculty of Aerospace Engineering at the Delft University of Technology, for financial support in establishing the experimental setup. We also give special thanks to S. Bernardy, P. Duyndam, D. Bruikman, and F. D. Duyvis for their technical assistance.

APPENDIX A: CHARACTERIZATION OF THE WALL-NORMAL BLOWING JET ACTUATOR

Since the aim of control is to manipulate large-scale structures in the logarithmic region, the actuator should have enough control authority in the logarithmic region of the TBL, where LSMs are most energetic. Thus, the actuator jet in crossflow needs to trail within this region to achieve a proper interaction. The jet flow may not reach a sufficient height when the jet exit velocity, v_{j}, is too low, while if v_{j} is too high the jet's trajectory may penetrate the edge of the boundary layer, thereby altering the free-stream flow. To study how the jet trajectory depends on its exit velocity, a characterization experiment was conducted. The wall-normal jet flow was operated in a continuous on-state at several velocity ratios, $r = v_{\mathrm{j}}/U_\infty$. The mean velocity field was inferred from 2D2C PIV performed with 2000 image pairs, and over a FOV spanning roughly 1.8δ in x and 0.35δ in y. The trajectory of the jet is taken as the streamline emanating from the center of the jet exit plane, as shown in Fig. 17(a) for several velocity ratios. It is evident that the two highest velocity ratios of $r = 0.5$ and 0.6 result in trajectories penetrating the upper edge of the logarithmic region (here indicated with the dashed line at $y/\delta = 0.2$) within $x/\delta < 0.5$. As expected, with a lower velocity ratio of $r = 0.4$, the jet trajectory remains within the logarithmic region for a prolonged distance ($\approx 1\delta$) and is therefore adopted in the current study. The momentum coefficient for $r = 0.4$

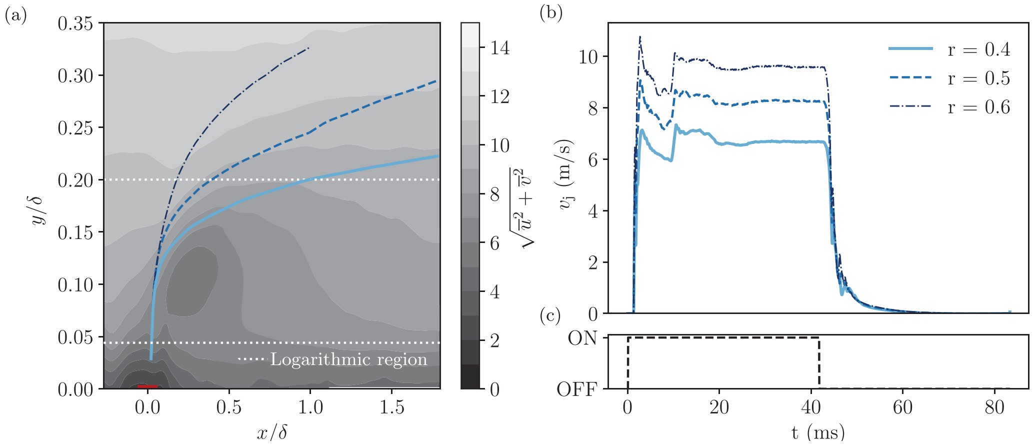

FIG. 17. (a) Trajectories of the wall-normal jet actuator flow within the grazing TBL flow, for three different velocity ratios. Lower and upper bounds of the logarithmic region are also indicated. A filled contour in the background shows the magnitude of in-plane velocity for the $r = 0.4$ case; the jet exit slit is indicated with a red line. (b) Phase-averaged jet exit velocity over 2048 on/off cycles. (c) Periodic valve command over one period of $T_j = 1/f_j \approx 83$ ms.

is $C_\mu = (\rho_\mathrm{j} v_\mathrm{j}^2 l_\mathrm{j})/(\rho_\infty U_\infty^2 \delta) = 0.75$, with $l_\mathrm{j} = 0.15$ mm being the length of the jet exit-slit. Velocity ratios lower than $r \leqslant 0.3$ cause the plume to remain within the logarithmic region for a longer streamwise extent. However, the feed system, including a pressure regulator, was not able to produce a stationary flow across the slit, as relatively large velocity fluctuations were observed over time.

Latency is essential to consider in designing an opposition control system, for timing purposes as well as the frequency response of the jet actuator. The hardware latency associated with the time it takes for the compressed air to accelerate through the valve, pneumatic tubing and flow conditioners, was quantified with an experiment: the valve was operated at a constant frequency f_j, with a 50% duty cycle (for a total duration of 2048 periods). This frequency was based on a statistical timescale of the LSMs, following $f_\mathrm{j} = U_c/(2l_\mathrm{LSM}) \approx 12$ Hz, where U_c is the convection velocity taken at the geometric center of the logarithmic region, $y_L^+ = 3.9\sqrt{\mathrm{Re}_\tau}$, and $l_\mathrm{LSM} = 6\delta$ is the statistical length of a high- or low-speed region [18,59]. A time series of the jet exit velocity was measured with HWA as described in Sec. II B, but with the difference being the use of a Dantec 55P11 probe. This probe was placed at $y = 3$ mm above the center of the jet exit slit. Phase-averaged responses of the jet exit velocity (with $t = 0$ being the instant of the valve on-command) over all periods are presented in Fig. 17(b). The velocity sharply rises approximately 1 ms after the on-command, and overshoots its steady-state value after roughly 3 ms. Subsequently, steady-state is reached at roughly 6 ms. When the valve receives the off-command, the shut down phase lasts for approximately 10 ms before the exit velocity returns to zero. It was confirmed that shortening the period of actuation did not alter the start- and shut-down transients. Hence, the maximum frequency for which an on- and off-state is reached is constrained by a 6 ms start-up time and a 10 ms shut-down time; this yields a frequency response of $f_\mathrm{act} \approx 63$ Hz.

APPENDIX B: SYSTEM IDENTIFICATION PROCEDURE

The linear coherence spectrum (LCS) evaluates the stochastic degree of coupling between the voltage fluctuations of the wall-mounted hot film, $e(t)$ (the input), and the streamwise velocity fluctuations within the logarithmic region, $u(t)$ (the output), as a function of the streamwise

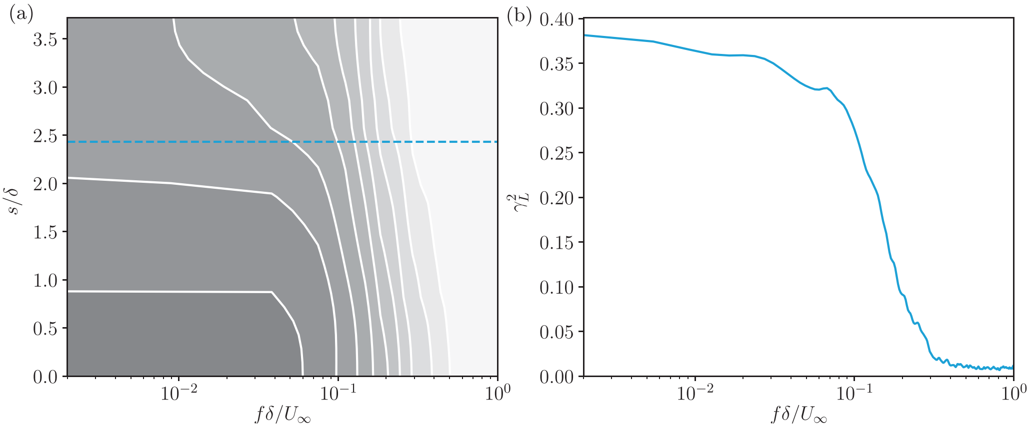

FIG. 18. (a) Spectrogram of $\gamma_L^2(f, s)$, as a function of frequency and the separation distance s between the wall-mounted hot film and velocity fluctuations in the logarithmic region. Filled isocontours correspond to magnitudes of 0.05:0.05:0.5. (b) One coherence spectrum for $s = 2.4\delta$.

separation distance s. The LCS is defined as [60]

$$\gamma_L^2(f, s) = \frac{|\langle E(f)U^*(f, s)\rangle|^2}{|\langle E(f)\rangle|^2|\langle U(f, s)\rangle|^2}, \tag{B1}$$

where $|\cdot|$ denotes the modulus. Here $E(f)$ and $U(f, s)$ are the temporal FFT's of the input and output signals, respectively. The coherence is bounded by 0 (no coherence) and 1 (perfectly coherent) and is presented in Fig. 18(a) as a function of $f\delta/U_\infty$ and separation distance, s/δ. With an increase in s, the coherence decays only marginally and its maximum value at low frequencies still remains at a level beyond 0.35 at the most downstream position. Figure 18(b) shows the LCS for $s = 2.4\delta$ in specific, which corresponds to the sensor-actuator spacing that was implemented (the reasoning for this is provided in Sec. III C). Figure 18(b) shows an initial trend of coherence that is nearly constant for low frequencies up to $f\delta/U_\infty \approx 0.1$ with $\gamma_L^2 \approx 0.3$, which is proven to be a sufficient coherence-magnitude for an opposition control scheme on the large-scale energy (in terms of its binary accuracy, see Sec. III D). Coherence drops sharply for smaller scales beyond $f\delta/U_\infty \gtrsim 0.1$, which renders it impossible to actuate upon those turbulence scales.

An input-output relation can be inferred from a calibration experiment to relate the input's voltage fluctuations to the velocity fluctuations at the downstream target-point (see Fig. 3); allowing for an LSE of the latter during real-time control. Given the presence of significant coherence, the linear transfer kernel, $H_L(f)$, will relate an estimate of the output (denoted with a hat) and the input signal in the frequency domain, following

$$\widehat{U}(f, s) = H_L(f, s)E(f). \tag{B2}$$

The complex-valued kernel has a frequency-dependent gain and phase, given by

$$|H_L(f, s)| = \frac{|\langle E(f)U^*(f, s)\rangle|}{\langle |E(f)|^2\rangle}, \text{ and} \tag{B3}$$

$$\phi_H(f, s) = \arctan\left\{\frac{\mathcal{I}[\langle E(f)U^*(f, s)\rangle]}{\mathcal{R}[\langle E(f)U^*(f, s)\rangle]}\right\}, \tag{B4}$$

where $\langle E(f)U^*(f, s)\rangle$ is the input-output cross-spectrum.

[1] S. J. Kline, W. C. Reynolds, F. A. Schraub, and P. W. Runstadler, The structure of turbulent boundary layers, J. Fluid Mech. **30**, 741 (1967).
[2] R. E. Falco, Coherent motions in the outer region of turbulent boundary layers, Phys. Fluids **20**, S124 (1977).
[3] K. C. Kim and R. J. Adrian, Very large-scale motion in the outer layer, Phys. Fluids **11**, 417 (1999).
[4] J. H. Lee and H. J. Sung, Very-large-scale motions in a turbulent boundary layer, J. Fluid Mech. **673**, 80 (2011).
[5] J. Jiménez, Coherent structures in wall-bounded turbulence, J. Fluid Mech. **842**, P1 (2018).
[6] R. Rathnasingham and K. S. Breuer, System identification and control of a turbulent boundary layer, Phys. Fluids **9**, 1867 (1997).
[7] S. F. Tardu, Near wall turbulence control by local time periodical blowing, Exp. Therm Fluid Sci. **16**, 41 (1998).
[8] R. Rathnasingham and K. S. Breuer, Active control of turbulent boundary layers, J. Fluid Mech. **495**, 209 (2003).
[9] H. L. Bai, Y. Zhou, W. G. Zhang, S. J. Xu, Y. Wang, and R. A. Antonia, Active control of a turbulent boundary layer based on local surface perturbation, J. Fluid Mech. **750**, 316 (2014).
[10] Z. X. Qiao, Y. Zhou, and Z. Wu, Turbulent boundary layer under the control of different schemes, Proc. Math. Phys. Eng. Sci. **473**, 20170038 (2017).
[11] P. Orlandi and J. Jiménez, On the generation of turbulent wall friction, Phys. Fluids **6**, 634 (1994).
[12] J. M. Hamilton, J. Kim, and F. Waleffe, Regeneration mechanisms of near-wall turbulence structures, J. Fluid Mech. **287**, 317 (1995).
[13] J. Jimenez and A. Pinelli, The autonomous cycle of near-wall turbulence, J. Fluid Mech. **389**, 335 (1999).
[14] W. Schoppa and F. Hussain, A large-scale control strategy for drag reduction in turbulent boundary layers, Phys. Fluids **10**, 1049 (1998).
[15] J. Canton, R. Örlü, C. Chin, and P. Schlatter, Reynolds number dependence of large-scale friction control in turbulent channel flow, Phys. Rev. Fluids **1**, 081501(R) (2016).
[16] J. Canton, R. Örlü, C. Chin, N. Hutchins, J. Monty, and P. Schlatter, On large-scale friction control in turbulent wall flow in low Reynolds number channels, Flow, Turbul. Combust. **97**, 811 (2016).
[17] I. Marusic, D. Chandran, A. Rouhi, M. K. Fu, D. Wine, B. Holloway, D. Chung, and A. J. Smits, An energy-efficient pathway to turbulent drag reduction, Nat. Commun. **12**, 5805 (2021).
[18] N. Hutchins and I. Marusic, Evidence of very long meandering features in the logarithmic region of turbulent boundary layers, J. Fluid Mech. **579**, 1 (2007).
[19] R. Deshpande, D. Chandran, A. J. Smits, and I. Marusic, The relationship between manipulated inter-scale phase and energy-efficient turbulent drag reduction, J. Fluid Mech. **972**, A12 (2023).
[20] I. Marusic, R. Mathis, and N. Hutchins, Predictive model for wall-bounded turbulent flow, Sci. Mag. **329**, 193 (2010).
[21] W. J. Baars, K. M. Talluru, N. Hutchins, and I. Marusic, Wavelet analysis of wall turbulence to study large-scale modulation of small scales, Exp. Fluids **56**, 188 (2015).
[22] S. L. Brunton and B. R. Noack, Closed-loop turbulence control: Progress and challenges, Appl. Mech. Rev. **67**, 050801 (2015).
[23] H. Choi, P. Moin, and J. Kim, Active turbulence control for drag reduction in wall-bounded flows, J. Fluid Mech. **262**, 75 (1994).
[24] A. Guseva and J. Jiménez, Linear instability and resonance effects in large-scale opposition flow control, J. Fluid Mech. **935**, A35 (2022).
[25] H. Rebbeck and K.-S. Choi, Opposition control of near-wall turbulence with a piston-type actuator, Phys. Fluids **13**, 2142 (2001).
[26] H. Rebbeck and K.-S. Choi, A wind-tunnel experiment on real-time opposition control of turbulence, Phys. Fluids **18**, 035103 (2006).
[27] M. R. Abbassi, W. J. Baars, N. Hutchins, and I. Marusic, Skin-friction drag reduction in a high-Reynolds-number turbulent boundary layer via real-time control of large-scale structures, Int. J. Heat Fluid Flow **67**, 30 (2017).

[28] W. J. Baars, N. Hutchins, and I. Marusic, Self-similarity of wall-attached turbulence in boundary layers, J. Fluid Mech. **823**, R2 (2017).

[29] C. E. Tinney, F. Coiffet, J. Delville, A. M. Hall, P. Jordan, and M. N. Glauser, On spectral linear stochastic estimation, Exp. Fluids **41**, 763 (2006).

[30] W. J. Baars, N. Hutchins, and I. Marusic, Spectral stochastic estimation of high-Reynolds-number wall-bounded turbulence for a refined inner-outer interaction model, Phys. Rev. Fluids **1**, 054406 (2016).

[31] N. Renard and S. Deck, A theoretical decomposition of mean skin friction generation into physical phenomena across the boundary layer, J. Fluid Mech. **790**, 339 (2016).

[32] S. Deck, N. Renard, R. Laraufie, and P.-E. Weiss, Large-scale contribution to mean wall shear stress in high-Reynolds-number flat-plate boundary layers up to $\mathrm{Re}_\theta = 13650$, J. Fluid Mech. **743**, 202 (2014).

[33] K. Fukagata, K. Iwamoto, and N. Kasagi, Contribution of Reynolds stress distribution to the skin friction in wall-bounded flows, Phys. Fluids **14**, L73 (2002).

[34] M. P. Schultz and K. A. Flack, The rough-wall turbulent boundary layer from the hydraulically smooth to the fully rough regime, J. Fluid Mech. **580**, 381 (2007).

[35] M. Hultmark and A. J. Smits, Temperature corrections for constant temperature and constant current hot-wire anemometers, Meas. Sci. Technol. **21**, 105404 (2010).

[36] B. L. Smith, D. R. Neal, M. A. Feero, and G. Richards, Assessing the limitations of effective number of samples for finding the uncertainty of the mean of correlated data, Meas. Sci. Technol. **29**, 125304 (2018).

[37] K. A. Chauhan, P. A. Monkewitz, and H. M. Nagib, Criteria for assessing experiments in zero pressure gradient boundary layers, Fluid Dyn. Res. **41**, 021404 (2009).

[38] N. Hutchins, T. B. Nickels, I. Marusic, and M. S. Chong, Hot-wire spatial resolution issues in wall-bounded turbulence, J. Fluid Mech. **635**, 103 (2009).

[39] A. J. Smits, J. Monty, M. Hultmark, S. C. C. Bailey, N. Hutchins, and I. Marusic, Spatial resolution correction for wall-bounded turbulence measurements, J. Fluid Mech. **676**, 41 (2011).

[40] M. Lee and R. D. Moser, Direct numerical simulation of turbulent channel flow up to $\mathrm{Re}_\tau = 5200$, J. Fluid Mech. **774**, 395 (2015).

[41] T. H. New, T. T. Lim, and S. C. Luo, Elliptic jets in cross-flow, J. Fluid Mech. **494**, 119 (2003).

[42] R. Sau and K. Mahesh, Dynamics and mixing of vortex rings in crossflow, J. Fluid Mech. **604**, 389 (2008).

[43] K. Mahesh, The interaction of jets with crossflow, Annu. Rev. Fluid Mech. **45**, 379 (2013).

[44] E. J. Gutmark, I. M. Ibrahim, and S. Murugappan, Circular and noncircular subsonic jets in cross flow, Phys. Fluids **20**, 075110 (2008).

[45] P. Pokharel and S. Acharya, Dynamics of circular and rectangular jets in crossflow, Comput. Fluids **230**, 105111 (2021).

[46] N. Hutchins, K. Chauhan, I. Marusic, J. Monty, and J. Klewicki, Towards reconciling the large-scale structure of turbulent boundary layers in the atmosphere and laboratory, Boundary-Layer Meteorol **145**, 273 (2012).

[47] E. Martini, J. Jung, A. V. G. Cavalieri, P. Jordan, and A. Towne, Resolvent-based tools for optimal estimation and control via the Wiener–Hopf formalism, J. Fluid Mech. **937**, A19 (2022).

[48] J. Jimenez, R. Martinez-Val, and M. Rebollot, Hot-film sensors calibration drift in water, J. Phys. E **14**, 569 (1981).

[49] D. R. Smith, Interaction of a synthetic jet with a crossflow boundary layer, AIAA J. **40**, 2277 (2002).

[50] M. E. Erengil and D. S. Dolling, Unsteady wave structure near separation in a Mach 5 compression ramp interaction, AIAA J. **29**, 728 (1991).

[51] J.-M. Shi, D. Gerlach, M. Breuer, and F. Durstb, Analysis of heat transfer from single wires close to walls, Phys. Fluids **15**, 908 (2003).

[52] E. S. Zanoun, F. Durst, and J. M. Shi, The physics of heat transfer from hot wires in the proximity of walls of different materials, Int. J. Heat Mass Transf. **52**, 3693 (2009).

[53] K. U. Kempaiah, F. Scarano, G. E. Elsinga, B. W. van Oudheusden, and L. Bermel, 3-dimensional particle image velocimetry based evaluation of turbulent skin-friction reduction by spanwise wall oscillation, Phys. Fluids **32**, 085111 (2020).

[54] B. Sun, M. Shehzad, D. Jovic, C. Cuvier, C. Willert, Y. Ostovan, J.-M. Foucaut, C. Atkinson, and J. Soria, Distortion correction of two-component two-dimensional PIV using a large imaging sensor with

application to measurements of a turbulent boundary layer flow at $\mathrm{Re}_\tau = 2386$, Exp. Fluids **62**, 183 (2021).

[55] I. Marusic, K. Chauhan, V. Kulandaivelu, and N. Hutchins, Evolution of zero-pressure-gradient boundary layers from different tripping conditions, J. Fluid Mech. **783**, 379 (2015).

[56] S. B. Pope, *Turbulent Flows* (Cambridge University Press, Cambridge, UK, 2000).

[57] P. T. Harsha and S. C. Lee, Correlation between turbulent shear stress and turbulent kinetic energy, AIAA J. **8**, 1508 (1970).

[58] N. Kasagi and K. Fukagata, The FIK identity and its implication for turbulent skin friction control, in *Transition and Turbulence Control*, Lecture Notes Series Institute for Mathematical Sciences National University of Singapore Vol. 8, edited by M. GadElHak and H. M. Tsai (World Scientific, Singapore, 2006).

[59] W. J. Baars and I. Marusic, Data-driven decomposition of the streamwise turbulence kinetic energy in boundary layers. Part 1. Energy spectra, J. Fluid Mech. **882**, A25 (2020).

[60] J. S. Bendat and A. G. Piersol, *Random Data: Analysis and Measurement Procedures*, 3rd ed. (John Wiley & Sons, New York, NY, 2000).